Department of Physics and Astronomy

University of Heidelberg

Master thesis

in Physics

submitted by

Fiona Sieber

born in Osnabrück

2024

Optimisation of a Nonlinear Pulse Compression Multi-Pass Cell

This Master thesis has been carried out by Fiona Sieber

at the

Max-Planck-Institut für Kernphysik

under the supervision of

apl. Prof. Dr. José R. Crespo López-Urrutia

Optimisierung der nichtlinearen Pulskompression in einer Multi-Pass-Zelle

Mit dem Ziel Präzisionsspektroskopie an hochgeladenen Ionen durchzuführen, transferrieren wir einen Frequenzkamm vom Nahinfraroten über die Erzeugung hoher Harmonischer ins extrem ultraviolette. Um die Ausbeute der hohen Harmonischen zu steigern, verbreitern wir die nahinfraroten Pulse spektral für eine zeitliche Pulskompression.

In einer Multi-Pass-Zelle mit Herriott-Konfiguration werden die Pulse in einen nichtlinearen Kristall fokussiert, wo sie Selbstphasenmodulation erfahren. Wiederholte Durchgänge verbreitern das Spektrum schrittweise, während die Materialdispersion durch gechirpte Spiegel teilweise kompensiert wird. Um die komprimierten Pulse zu charakterisieren und zu optimieren, wird ein Frequency Resolved Optical Gating (FROG) Aufbau entworfen und implementiert.

Die eingehenden Pulse besitzen eine Pulsdauer von 225 fs, Satellitenpulse und eine kubische spektrale Phase. Darüber hinaus werden die Leistungsverluste der leeren Multi-Pass-Zelle um 38% verringert; auf eine Transmission von 92%. Yttrium-Aluminium-Granat verbreitert das Spektrum um einen Faktor von zwei, wobei vorherige Ergebnisse mit Quarzglas um 15% übertroffen werden. Bemerkenswert ist die stabile Ausgangsleistung der Multi-Pass-Zelle. Ein erstes FROG-Spektrogramm zeigt, dass die Pulse einen räumlichen Chirp in oder nach der Multi-Pass-Zelle aufsammeln, was weiterer Untersuchung bedarf.

Die spektrale Verbreiterung ist vielversprechend, um in einer zukünftigen Post-Kompression die mit Quarzglas erzielte Pulsdauer von 90 fs zu unterbieten. Darüber hinaus ermöglicht ein breiteres Spektrum die Anregung einer größeren Anzahl von Übergängen in hochgeladenen Ionen.

Optimisation of a Nonlinear Pulse Compression Multi-Pass Cell

Striving for precision spectroscopy on highly charged ions (HCI), we employ high harmonic generation (HHG) to transfer a near-infrared (NIR) frequency comb to the extreme ultraviolet (XUV). Aiming to increase the harmonic yield, we spectrally broaden the NIR pulses for temporal compression.

Within a Herriott-type multi-pass cell (MPC), pulses are focused into a nonlinear crystal, where they experience self-phase modulation. Multiple passes incrementally broaden the spectrum, while the material dispersion is partially compensated using chirped mirrors. To characterise the compressed pulses and optimise them, a set-up for Frequency Resolved Optical Gating (FROG) is designed and implemented. The initial pulses exhibit a duration of 225 fs featuring satellite pulses; their spectral phase is cubic. Further, we reduce the empty MPC's power losses by 38%, reaching a total transmission of 92%. Yttrium aluminium garnet broadens the spectrum by a factor of two, surpassing our previous results with fused silica by 15%. Notably, the cell output power remains stable. A first FROG trace reveals that the pulses become spatially chirped in or after the MPC, requiring further investigation.

Looking ahead, the spectral broadening is promising for a future post-compression with pulse durations well below the previously obtained 90 fs. Additionally, a broader spectrum enables access to a wider range of HCI transitions.

Contents

1 Introduction

1.1 Precision spectroscopy

Laser precision spectroscopy is a quickly advancing domain in physics. It provides a deeper understanding of fundamental physics, such as interactions between the atomic core and shell electrons, nuclear dipole moments [1] or a possible variation of the fine-structure constant α [2]. Another application is building even more precise clocks than the current time standard; at PTB in Germany a Caesium fountain clock with an uncertainty of six billionths of a second per year [3]. More precise clocks open the way for understanding various fundamental phenomena which cause frequency shifts at relative frequency uncertainty of below 10^{-18} [1]. One of them is the gravitational redshift which could be observed across a 1 mm height difference with a strontium lattice clock [5]. The degree of attainable information about fundamental phenomena scales with precision, accordingly researchers make a lot of effort to that extent. The relative frequency uncertainty of a clock is inversely proportional to its transition frequency, therefore choosing transitions with high frequencies is profitable. From the standard microwave regime (up to 3×10^{11} Hz) one could switch to transitions from the near-infrared (NIR) (2.4×10^{14} Hz to 4×10^{14} Hz) up to the x-ray regime (from 3×10^{16} Hz to 3×10^{19} Hz) [6], [7]. One challenge is to generate and determine NIR to x-ray frequencies accurately as they are orders of magnitudes faster than can be electronically counted. Further, an extremely narrow atomic transition has to be excited. To these extents the development of the frequency comb has been essential. [8]

---

[1] 10^{-18} is a relative frequency uncertainty for a quantum-logic clock with a single aluminum ion [4]

1.2 Frequency comb

Electronic transitions in and beyond the optical regime are interesting candidates for more precise atomic clocks and other applications. Therefore measuring these frequencies accurately is desirable, but as nearly 5×10^{14} oscillations per second can not be counted electronically, other solutions have to be found. In metrology laboratories highly complex harmonic frequency chains filling several rooms were engineered for the sole purpose of measuring one particular optical frequency. Theodor W. Hänsch and John L. Hall saw the potential to replace these frequency chains with a frequency comb which granted them the nobel prize in 2005.[8]
For an infinite train of pulses with duration Δt, the Fourier transform gives distinctive peaks with equal spacing of the fixed pulse repetition frequency of the laser oscillator f_{rep} in the frequency domain. Exemplary for a pulse duration of $\Delta t = 50\,\mathrm{fs}$, the spectrum spans approximately $\Delta f = 20\,\mathrm{THz}$ which can be further broadened to 320 THz in a nonlinear optical medium [9]. The frequency f_n of the n-th comb tooth can be calculated from the repetition frequency f_{rep} and the carrier envelope offset frequency f_{CEO}

$$f_n = n f_{\mathrm{rep}} + f_{\mathrm{CEO}}. \tag{1.1}$$

The carrier envelope offset (CEO) frequency f_{CEO} results from the carrier to envelope phase ϕ_{CEP} which slips due to dispersion in a cavity from pulse to pulse. Such a pulse train in the time-domain is visualised in Figure 1.1 in the top panel. The bottom panel depicts the pulse train's comb-shape in the frequency domain. It is essential to determine the frequency offset f_{CEO} in order to know the exact frequency of every comb tooth. This can be achieved by first broadening the spectrum to span over an octave and then using a nonlinear crystal to frequency-double the lower frequency teeth. Those newly generated overtones contain twice f_{CEO}. Therefore, comparing them to the original comb lines using a beat note retrieves f_{CEO}. Stabilising the thus determined f_{CEO} will stabilise each comb tooth.

Due to this exact and absolute knowledge of every comb tooth's frequency, a frequency comb is the analogue of a ruler in precision spectroscopy. It can be tuned, e.g. to match an atomic transition, via both its repetition rate and its

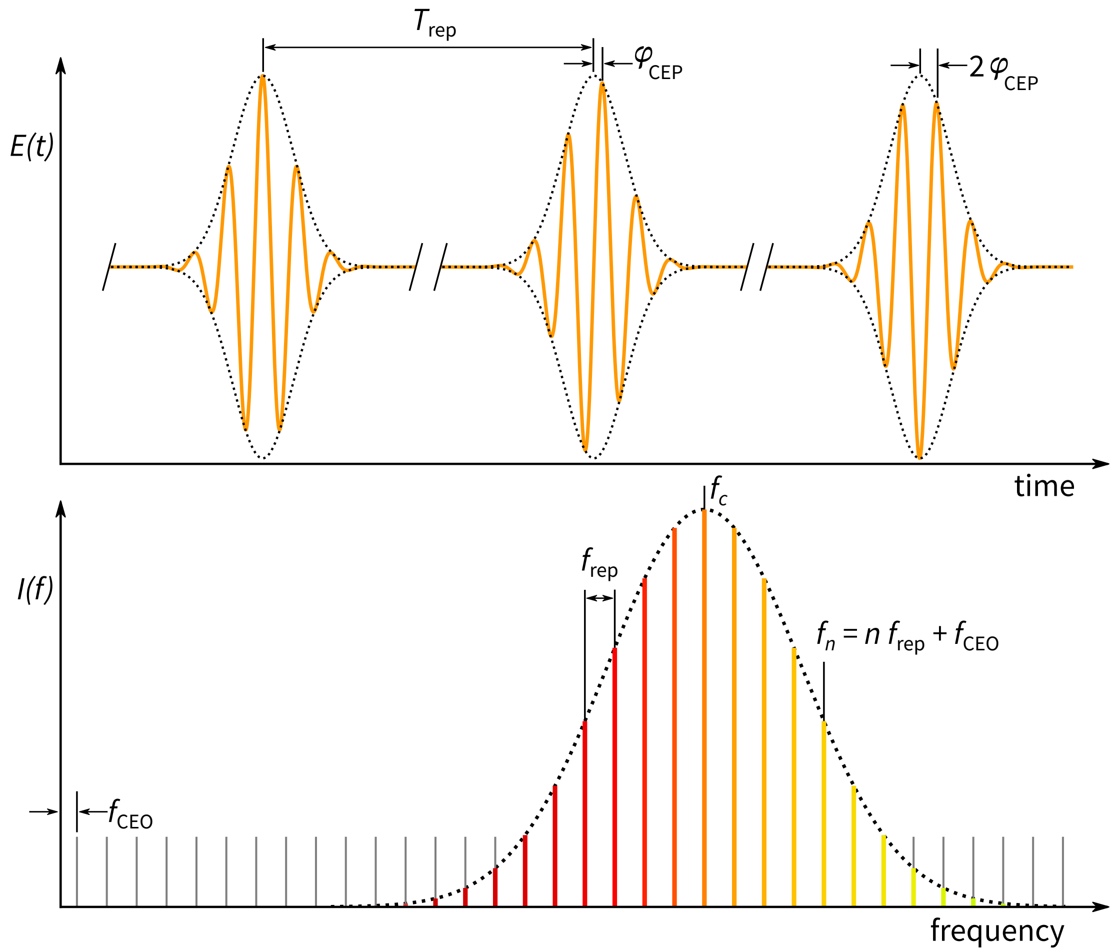

Figure 1.1: A frequency comb in the time (top) and frequency domain (bottom). The real part of the electric field is depicted as pulses with the same envelope (dashed line) and repetition rate $f_{\text{rep}} = 1/T_{\text{rep}}$. The carrier offset phase ϕ_{CEP} slips from pulse to pulse. The intensity of the frequency peaks follows the envelope centered at the carrier frequency $f_c = \omega_c/(2\pi)$. Figure from [10].

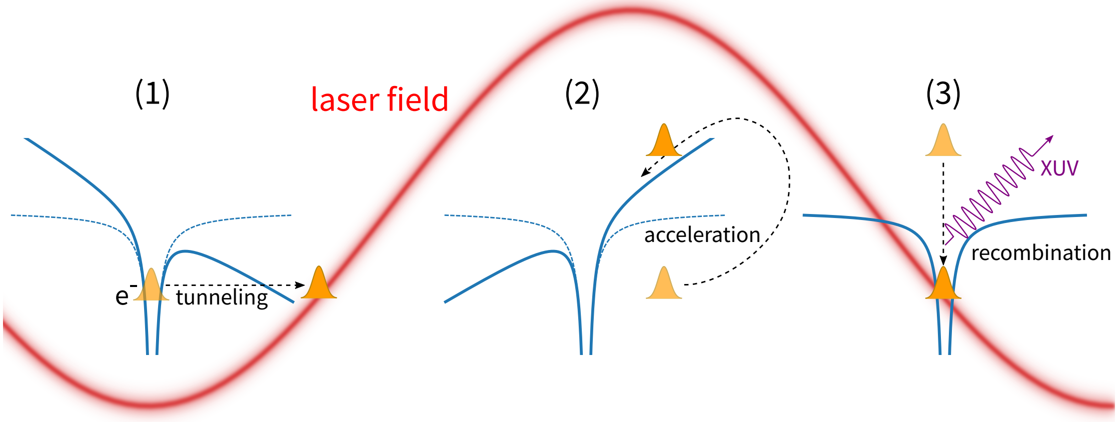

Figure 1.2: Schematic of the semi-classical three-step model for HHG. (1) Tunnel ionisation of an atom in a very strong electromagnetic field. (2) Trajectory of the free electron which reverses its direction after half of an optical period. (3) Recombination of the returned electron and ion under emission of a high energetic photon. Figure from [10]

carrier envelope offset.
[1], [8], [9]

XUV frequency comb Briefly summarised, an XUV frequency comb is based on the transfer of a commercial NIR frequency comb to the XUV employing high harmonic generation (HHG). The HHG process can be understood in a semi-classical manner following the three-step model in Figure 1.2 for atomic gases. An intense laser field modifies the Couloumb potential of an atom such that an electron might tunnel through. The free electron in the oscillating laser field follows a classical trajectory. For a suitable time of the tunnel emission the trajectory might bring the free electron back to the atom. In a recombination process a high energy photon is emitted. [10], [11], [12], [13]

1.3 Vision of the experiments at MPIK

The goal of the experiments, led by J. R. Crespo López-Urrutia at the Max-Planck-Institut für Kernphysik (MPIK), is precision spectroscopy on highly charged ions (HCI). HCI are interesting to study, as their atomic transitions being scantly sensitive to external electro-magnetic fields and black body radiation, have the potential to be measured with an extremely high precision. Atomic transition frequencies depend on the fine structure constant α whose possible variation is fascinating to probe as it is required in some higher dimensional models to unify gravity with the other three forces of nature [14]. A challenge using HCI is that the majority of them inhibit no metastable states in the optical regime necessary for laser cooling. Further, their highly forbidden, thus spectrally very narrow, transitions are shifted to the extreme ultraviolet (XUV) where there are no coherent light sources available to probe transitions with the desired accuracy. [14]

Therefore, at MPIK the expertise from the production of HCI in an electron beam ion trap (EBIT), the trapping and cooling in a linear Paul trap and XUV spectroscopy will be combined in the beamline shown in Figure 3.1. In a compact EBIT at room-temperature, an electron-beam can ionise atoms up to iron to the hydrogen-like state and atoms up to xenon to the helium-like and lithium-like state. [15] Afterwards, a deceleration beam line leads to a superconducting linear Paul trap which traps the HCI in a laser-cooled beryllium $^{9}\mathrm{Be}^{+}$ crystal where they are sympathetically cooled down to the mK regime [16]. Currently in progress are further improvements of this set-up aiming for ground state cooling of HCI [17]. The future goal is its connection to an XUV frequency comb to perform spectroscopy on the HCI. We currently work on realising a stable operation of the XUV frequency comb. To this extent, this work aims to provide a suitable and well-defined laser pulse for HHG.

1.4 Motivation

To increase the HHG yield, beforehand compressing the pulse in the time domain is favourable. We have implemented a pulse compression scheme based on the Kerr effect in a nonlinear medium using a multi-pass approach. This work aims to optimise this pulse compression multi-pass cell (MPC) with the aid of pulse characterisation. For the pulse characterisation part, I designed and built a Frequency Resolved Optical Gating (FROG) set-up. For the pulse compression part, I implemented several improvements, such as a change of the nonlinear medium.

Why are shorter pulses advantageous for us? Aiming for precision spectroscopy on HCI, we employ the HHG process whose yield increases with the pulse's peak power. For a fixed average power, the pulse's peak power can be enhanced by reducing the pulse duration. Moreover, a shorter pulse duration decreases the gas ionisation which takes place before the intensity level for HHG is reached. This in turn decreases ionisation-induced effects, further improving the HHG yield [18]. A higher yield favors attaining higher harmonic orders. Another advantage appears from the fourier-linked broader spectrum of a time-shortened pulse: The frequency comb transferred from the NIR to the XUV also covers a broader spectral range, thereby attaining more HCI transitions.
The main advantage of temporal pulse compression in an MPC instead of in waveguides is a high power compatibility as the critical power of self-focusing of a nonlinear medium can be exceeded. Additionally, it promotes spatial homogeneity of the beam. [19]

Why is pulse characterisation necessary? Pulse characterisation provides valuable spectral, temporal and phase information. The pulse shape and duration notably impact its peak power and, consequently, the yield of HHG. By employing pulse characterisation before and after our MPC, we can effectively monitor the achieved spectral broadening and temporal compression.

1.5 Starting point

Previously, our group had obtained first pulse compression results with the MPC by using an autocorrelator to measure the pulse duration. The MPC with two

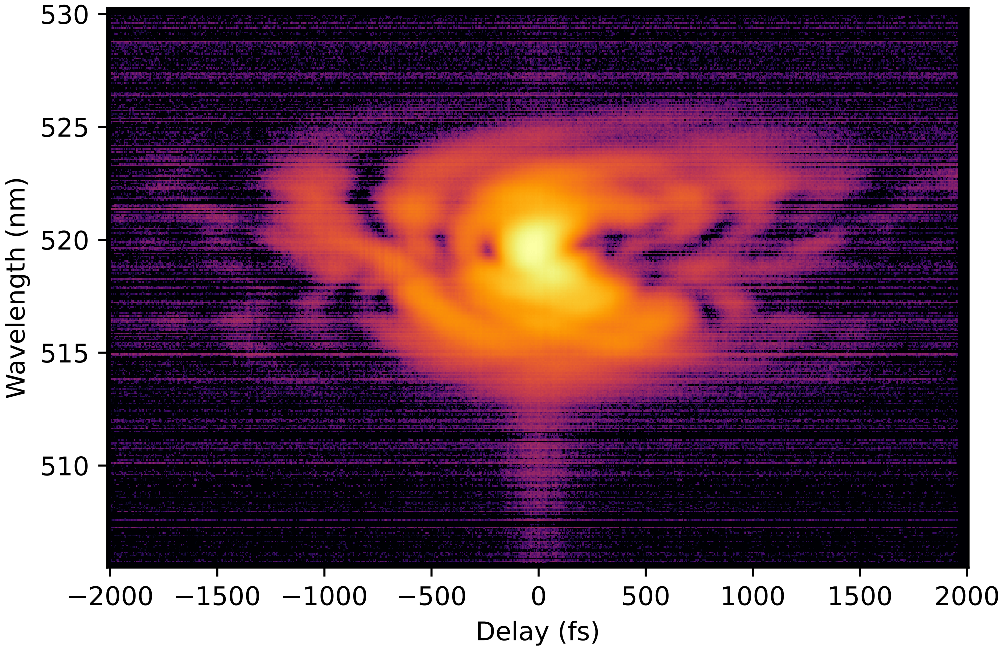

Figure 1.3: Previous FROG trace. For each time delay between the pulse and it's copy a spectrum is shown in a logarithmic colour scale. Its inherent feature, a symmetry with respect to zero delay, is violated. Presumably the experimental realisation was the cause. [21]

plates of fused silica, each 6.35 mm thick, compressed the pulse at 55 W average power to ∼ 90 fs [10], [20]. Our big aim is to compress the pulse even further, to around 30 fs. To this extent, firstly, we need to attain stable output powers for input powers exceeding 55 W. Secondly, improving the power transmission, which was only ∼ 85% for the empty cell [20], is desirable. Therefore, a more accurate and detailed pulse characterisation before and after the MPC is essential.

Before this work, in 2022, pulse characterisation was only possible based on retrieval from an asymmetric, noisy FROG trace in Figure 1.3 which yielded a pulse duration of (183 ± 3) fs before the MPC [21].

Even though several measurements yielded the same trace, necessitating profound noise corrections the pulse shape is not accurately retrieved. This works aims to obtain more symmetric and less noisy experimental data.

1.6 Approach

To improve the temporal compression in the MPC, in this work we employ YAG instead of fused silica, since it has a higher nonlinear coefficient. Additionally, we customised new curved mirrors for the MPC which have a higher reflectivity and negative group delay dispersion (GDD). Dispersion-induced temporal broadening of the pulse reduces the highly intensity dependent nonlinear interaction pass by pass. Therefore, a partial direct chirp compensation should ensure improvements in efficiency. Further, improving the mode-matching before and the alignment in the MPC is a part of this work.

For the pulse characterisation, I designed and realised a FROG set-up. One main improvement is a reduced distance between its components[2] for a higher experimental accuracy. Moreover, the set-up is placed on a separate breadboard which can be flexibly removed. In a next step, the noise correction of the FROG data and the subsequent pulse retrieval is studied.

This thesis begins with an overview of the theoretical background, followed by a description of the experimental set-up. The subsequent section presents and analyses the experimental results, leading to a conclusion and a discussion of future prospects.

---

[2] reduced distance between the split-and-delay line and the BBO crystal

2 Theoretical Background

2.1 Ultrashort laser pulses

2.1.1 Wave description

Light in vacuum fulfills the electromagnetic wave equation

$$\nabla^2 \vec{E} - \frac{1}{c_0^2} \frac{\partial^2 \vec{E}}{\partial t^2} = 0 \tag{2.1}$$

where the electric field $\vec{E}(t, \vec{r})$ depends on the time t and position $\vec{r}$. c_0 is the speed of light in vacuum, which is fundamentally related to the electric ϵ_0 and magnetic constant μ_0 with $c_0 = 1/\sqrt{\epsilon_0 \mu_0}$. For an electromagnetic wave in matter, the velocity of light c, the electric permittivity ϵ and magnetic permeability μ in the medium have to be taken into account. They are connected to the refractive index n with $c/n = 1/\sqrt{\epsilon\mu}$. Further, in matter a polarisation or magnetisation of the medium and source properties can play a role, as will be explained in the following chapter about nonlinear optics.

Remaining in the vacuum case, the electromagnetic wave equation has a simple, real solution which is a monochromatic plane wave

$$\vec{E}(\vec{r}, t) = \vec{E}_0(\vec{r}) \cdot \cos(\omega t - \vec{k}\vec{r} + \phi(\vec{r})) \tag{2.2}$$

with amplitude $\vec{E}_0$, angular frequency ω, wavevector $\vec{k}$ and position dependent phase $\phi(\vec{r})$. A more general complex monochromatic solution is denoted by

$$\vec{\mathcal{E}}(\vec{r}, t) = \vec{\mathcal{E}}_0(\vec{r}) \cdot e^{i(\omega t - \vec{k}\vec{r})} \tag{2.3}$$

where the calligraphic representation illustrates the complex valuedness. The complex amplitude is given by $\vec{\mathcal{E}}_0(\vec{r}) = \vec{E}_0 \cdot e^{i\phi(\vec{r})}$. The real part of the Representation 2.3 equals the Solution 2.2. As the Wave Equation 2.1 is linear, the superposi-

tion principle is applicable. It states that two solutions $\vec{\mathcal{E}}(\vec{r}, t_1)$ and $\vec{\mathcal{E}}(\vec{r}, t_2)$ form another solution with scalars a and b as $\vec{\mathcal{E}}(\vec{r}, at_1 + bt_2) = a\vec{\mathcal{E}}(\vec{r}, t_1) + b\vec{\mathcal{E}}(\vec{r}, t_2)$. Therefore multiple solutions at different angular frequencies can be added to obtain more refined electric field shapes. This sets the basis for Fourier analysis.
[6], [22]

2.1.2 Fourier description

In the following the polarization (vectorial treatment) and spatial dependence of the electric field $E(t)$ are dropped for simplicity.
A complex spectrum of a time dependent function $E^+(t)$ can be defined through the Fourier transform

$$E^+(\omega) = \mathcal{F}\{E^+(t)\} = \int_{-\infty}^{\infty} E^+(t) e^{-i\omega t} dt. \tag{2.4}$$

Applying the inverse Fourier transform to the complex spectrum retrieves the time-dependency

$$E^+(t) = \mathcal{F}^{-1}\{E^+(\omega)\} = \frac{1}{2\pi} \int_{-\infty}^{\infty} E^+(\omega) e^{i\omega t} d\omega. \tag{2.5}$$

From the formalism of the inverse Fourier transform result negative frequency components. Therefore it is convenient to introduce a complex electric field $E^+(t)$ in a way that it is the Fourier transform of

$$E^+(\omega) = \begin{cases} E(\omega) & \omega \geq 0 \\ 0 & \omega < 0 \end{cases}. \tag{2.6}$$

With similarly defined $E^-(t)$ and $E^-(\omega)$ the real electric field $E(t)$ and its complex spectrum $E(\omega)$ are

$$\begin{aligned} E(t) &= E^+(t) + E^-(t), \\ E(\omega) &= E^+(\omega) + E^-(\omega). \end{aligned}$$

The complex spectrum can be written as a spectral amplitude $|E(\omega)|$ with a spectral phase $\phi(\omega)$

$$E(\omega) = |E(\omega)| \cdot e^{i\phi(\omega)}. \tag{2.7}$$

A similar representation is useful for the complex electrical field. A case with a spectral amplitude which is centered around a carrier frequency ω_c and whose magnitude is only significant in an interval $\Delta\omega \ll \omega_c$ is of interest in practice.[1] Therefore, one writes with the real field envelope $A(t)$ and complex field envelope $\mathcal{A}(t)$

$$E^+(t) = \frac{1}{2}A(t)e^{i(\phi_{\mathrm{CEP}}+\phi(t)+\omega_c t)} = \frac{1}{2}\mathcal{A}(t)e^{i\omega_c t}, \tag{2.8}$$

where the spectral phase is split into a time-independent "carrier envelope phase" ϕ_{CEP}, a carrier frequency contribution $\omega_c t$ and a time-dependent phase $\phi(t)$. The time derivative of the spectral phase is the instantaneous angular frequency $\omega(t)$ of the electric field

$$\omega(t) = \omega_c + \frac{d\phi(t)}{dt}. \tag{2.9}$$

If the last term is nonzero, the instantaneous frequency deviates from the carrier frequency. This is called a frequency modulation or chirp of the pulse. Therefore knowledge about the electric field's time-dependent spectral phase is the key in order to determine the chirp of a pulse. For a positive curvature of the spectral phase, $d^2\phi/dt^2 > 0$, the pulse is said to be up-chirped. A negative curvature implies a down-chirped pulse. Both of these cases are represented in Figure 2.1 where the real part of the electric field, its intensity and spectral phase are displayed in the time domain.
[23]

---

[1] If this condition is fulfilled the slowly varying envelope approximation is valid.

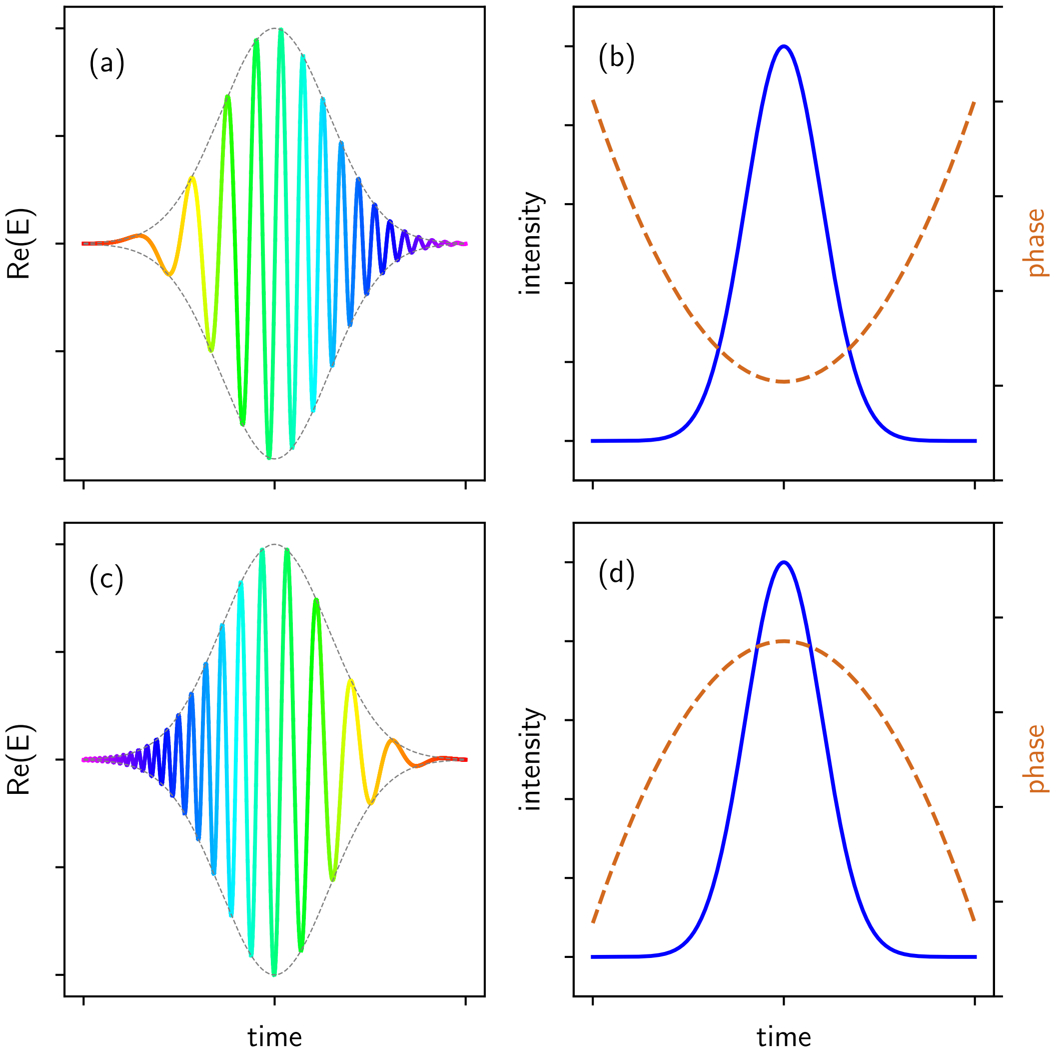

Figure 2.1: Illustration of an up- and down-chirped pulse. The real part of the electric field (a), the intensity (blue) and spectral phase (brown) (b) of the up-chirped pulse. Similarly, (c) and (d) for a down-chirped pulse. The rainbow colors illustrate the instantaneous frequencies. Figure from [24].

2.1.3 Dispersion

Generalising from the previously discussed vacuum case to light propagation in media, dispersion needs to be included in the description of the electrical field from Equation 2.3. In dispersive media, the index of refraction n is frequency dependent, leading to a speed of light in the medium of $c(\omega) = c_0/n(\omega)$. Consequently, the wavenumber k has to be replaced by the frequency dependent propagation constant

$$\beta = n(\omega)\frac{\omega}{c_0}, \tag{2.10}$$

simplifying to the one-dimensional case

$$\mathcal{E}(z,t) = \mathcal{E}_0(z) \cdot e^{i(\omega t - \beta z)}. \tag{2.11}$$

For ultrashort laser pulses, the propagation constant β is Taylor expanded around the pulses' carrier frequency ω_c

$$\beta(\omega) = \beta(\omega_c) \quad + (\omega - \omega_c) \underbrace{\left.\frac{d\beta}{d\omega}\right|_{\omega_c}}_{\substack{=v_g \\ \text{Group Velocity}}} \quad + \frac{1}{2}(\omega - \omega_c)^2 \underbrace{\left.\frac{d^2\beta}{d\omega^2}\right|_{\omega_c}}_{\substack{=\text{GVD} \\ \text{Group Velocity} \\ \text{Dispersion}}} \quad + \cdots$$

If the group velocity dispersion (GVD) is negligible, the group velocity v_g is the velocity at which the envelope of the pulse travels. A GVD will change the shape of the envelope, either broadening or shortening a pulse in the time-domain. If GVD > 0 the medium exhibits normal dispersion meaning higher frequency components travel slower than lower ones. This equals an up-chirp effect which is illustrated in Figure 2.1. The opposite occurs for anomalous dispersion with GVD < 0 equaling a down-chirp effect. A group delay dispersion (GDD) for a certain optical element with length l is defined as GDD $=$ GVD $\cdot\, l$ [25].
[22], [26]

2.1.4 Pulse shapes

In this work, the pulse duration τ_p is defined as the full width at half maximum (FWHM) of the temporal intensity profile $|A(t)|^2$. Similarly, the spectral width $\Delta\omega_p$ is defined as the FWHM of the spectral intensity profile $|A(\omega)|^2$. Some standard waveforms are listed in Table 2.2.

As the Fourier transform links the temporal and spectral shape of a pulse, also pulse duration τ_p and spectral width $\Delta\omega_p$ are connected by

$$\Delta\omega_p \cdot \tau_p \geq 2\pi \cdot c_B. \tag{2.12}$$

The minimum duration-bandwidth product depends on a numerical constant c_B which differs from pulse shape to pulse shape (see Table 2.2). The equality holds for so-called "Fourier limited" pulses which are unchirped.
[23]

Shape	Intensity profile	τ_p	Spectral profile	$\Delta\omega_p$	c_B
Gauss	$\exp(-2(t/\tau_G)^2)$	$1.177\tau_G$	$\exp(-(\omega\tau_G/2)^2)$	$2.355/\tau_G$	0.441
Sech^2	$\text{sech}^2(t/\tau_s)$	$1.763\tau_s$	$\text{sech}^2(\pi\omega\tau_s/2)$	$1.122/\tau_s$	0.315
Lorentz	$1/(1+(t/\tau_L)^2)$	$1.287\tau_L$	$\exp(-2\|\omega\|\tau_L)$	$0.693/\tau_L$	0.142

Table 2.2: Examples of standard pulse profiles. For each intensity profile its corresponding spectral profile, pulse duration τ_P, bandwidth $\Delta\omega_p$ and numerical constant c_B are listed. [23]

2.2 Nonlinear optics

In this chapter, the effects of placing a medium in a high intensity light field will be treated. From a macroscopic point of view, a dielectric material responds to an externally applied field $\vec{E}$ with a polarisation $\vec{P}$. This macroscopic polarisation is the sum of all atomic responses. For small external fields, the restoring atomic forces can be assumed to be proportional to the elongations of the electrons from their equilibrium positions. This is described by the model of the Lorentz Oscillator. For field strengths in the regime of atomic electric fields, approximately 5×10^{11} V/m, nonlinearities arise [26]. These nonlinearities are responsible e.g. for the dependence of a material's refractive index on the light intensity (Kerr effect) or the alteration of frequency when light passes through a medium. In general, the polarisation direction i and direction of the electric field are not identical. They are linked by a susceptibility tensor $\chi^{(n)}$ of n^{th} rank,

$$P_i = \varepsilon_0 \left(\sum_j \chi_{ij}^{(1)} E_j + \sum_{j,k} \chi_{ijk}^{(2)} E_j E_k + \sum_{j,k,l} \chi_{ijkl}^{(3)} E_j E_k E_l + ... \right). \tag{2.13}$$

The elements of the susceptibility tensor give the strength of the polarisation response. The elements rapidly decrease with increasing tensor order n. Therefore, to observe nonlinearities very intense electric fields, in the order of the interatomic electric fields 5×10^{11} V/m, have to be applied.

In the following, only parametric interactions are considered which excludes energy exchanges between the medium and the waves. Further, only stationary continuous waves, in contrast to pulsed light, are treated. Assuming a homogeneous, isotropic ($\vec{P} \parallel \vec{E}$) dielectric medium, the nonlinear wave equation

$$\nabla^2 \vec{E} - \frac{1}{c_0^2} \frac{\partial^2 \vec{E}}{\partial t^2} = \mu_0 \frac{\partial^2 \vec{P}}{\partial t^2}. \tag{2.14}$$

has to be satisfied. This can be rewritten as a nonlinear partial differential equation containing the speed of light in the medium with refractive index $n = c_0/c$ and the nonlinear part of the polarisation $\vec{P_{nl}} = \chi^{(2)} \vec{E}^2 + \chi^{(3)} \vec{E}^3 + ...$ where χ^n is the remaining element of the susceptibility tensors under the assumptions of isotropy and homogeneity.

Rewriting Equation 2.14 as

$$\nabla^2 \vec{E} - \frac{1}{c^2} \frac{\partial^2 \vec{E}}{\partial t^2} = -\vec{S},$$

allows the interpretation of

$$\vec{S} = -\mu_0 \frac{\partial^2 \vec{P_{nl}}}{\partial t^2}$$

as a source term which radiates into a linear medium with refractive index n. This nonlinear partial differential equation can be approached with the iterative Born Approximation or Coupled Wave Theory.
[22]

2.2.1 Second Harmonic Generation

The standard example of second harmonic generation (SHG) is frequency doubling of light in a nonlinear crystal. In this case, only the second order nonlinearity is of importance. Further assuming an incident monochromatic wave in z-direction $\vec{E} = \vec{E_0} \cdot \cos(\omega t - kz)$ with amplitude $\vec{E_0}$, angular frequency ω and wave vector $\vec{k} = k \cdot \vec{e_x}$, Equation 2.13 for the polarisation reduces to

$$P_x = \epsilon_0 \left(\chi^{(1)}_{xz} E_0 \cos(\omega t - kz) + \chi^{(2)}_{xzz} E_0^2 \cos^2(\omega t - kz) \right) . \tag{2.15}$$

Using $\cos^2 x = \frac{1}{2} (1 + \cos(2x))$ and dropping the indices of the susceptibility, one can constate that the polarisation contains three different terms:

$$P_x(z = 0) = \epsilon_0 \left(\chi^{(1)} E_0 \cos(\omega t) + \frac{1}{2} \chi^{(2)} E_0^2 + \frac{1}{2} \chi^{(2)} E_0^2 \cos(2\omega t) \right) . \tag{2.16}$$

The first term at angular frequency ω is responsible for Rayleigh scattering, the second one is a constant and the third one is the overtone wave at 2ω. This term, whose intensity scales proportionally to the intensity of the incident wave, is the one relevant for SHG. Figure 2.3 illustrates these different terms arising in the case of frequency doubling in a nonlinear crystal with the above simplifications.
These microscopic polarisations of the individual atoms have to be in phase at each location in the medium to interfere constructively to a macroscopic wave. Therefore, the phase velocity of the incident wave and its overtone in the medium must be equal which generally is not the case due to dispersion. There are different methods to compensate for the dispersion such as utilising the temperature dependence of the refractive index or birefringence. A birefringent crystal allows to tune the phase velocity which depends on the propagation direction, polarisation with respect to the crystal's optical axis and light frequency.
[1], [22]

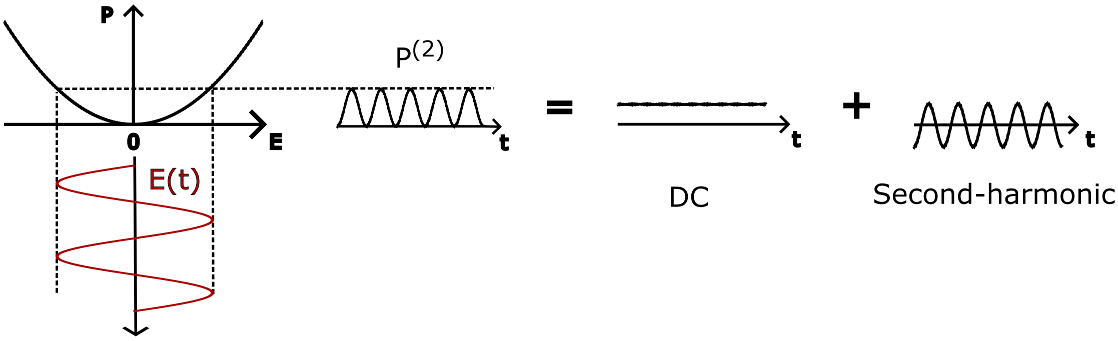

Figure 2.3: Illustration of SHG with a monochromatic sine-wave as incident wave in red. The second order polarisation can be split as in Equation 2.16 into a constant term and one oscillating at doubled frequency. Adapted from [22].

Phase-matching in a birefringent crystal

Phase-matching in the case of SHG refers to the phases of the fundamental wave and its overtone, as their constructive interference is essential for a macroscopic SHG signal. The critical phase-matching length l_c is defined as the distance after which the overtone shows a phase lack of π with respect to the fundamental wave,

$$l_c = \frac{\lambda_0}{2\left(n(2\omega) - n(\omega)\right)}. \tag{2.17}$$

This means that from the critical phase-matching length onwards the overtone interferes destructively until a distance of $2l_c$ is reached. [1]

Considering SHG as a photon interaction process, two photons, labelled one and two, from the incoming wave interact in the nonlinear medium to generate a third photon, labelled SHG. Conservation of energy is ensured by the frequency matching condition $\omega_1 + \omega_2 = \omega_{\mathrm{SHG}} = 2\omega$, the frequency of the second harmonic ω_{SHG} has to be twice the initial frequency of the photons $\omega = \omega_1 = \omega_2$. The momentum conservation reduces to the phase-matching condition for the wavevectors (in the medium)

$$\vec{k_1} + \vec{k_2} = \vec{k}_{\mathrm{SHG}}. \tag{2.18}$$

In the example above, two photons from the same beam interact, therefore $\vec{k_1} = \vec{k_2} = \vec{k}$ and $\vec{k}_{\mathrm{SHG}} = 2\vec{k}$.
The photon interaction picture highlights that there are nearly no limitations for employing SHG over wide spectral regions. Only phase-matching requirements and the medium's transparency pose minimal constraints.
[22]
For collinear SHG, one obtains from Equation 2.18

$$2\frac{\omega n(\omega)}{c_0} = \frac{\omega_{\mathrm{SHG}} n(\omega_{\mathrm{SHG}})}{c_0}, \tag{2.19}$$

by using $|\vec{k}| = \frac{\omega n(\omega)}{c_0}$. This yields the SHG phase-matching condition

$$n(\omega) = n(2\omega). \tag{2.20}$$

The refractive index n of the nonlinear material varies with the wave's frequency, a phenomenon known as dispersion. Consequently, the phase-matching condition for SHG is generally not satisfied. In practise, often birefringence of anisotropic media is used to compensate the effect of dispersion which is called critical phase-matching. The simplest anisotropic media are uniaxial media. Uniaxial refers the crystal exhibiting anisotropy along a single direction, the optical axis, while all directions perpendicular to it are equivalent. As light travels along the optical axis, all potential polarisations remain perpendicular to it. Therefore, the optical axis is known as the ordinary axis, inhibiting a polarisation-independent refractive index $n_o(\omega)$.Propagation directions that differ from the optical axis are termed extraordinary, as the refractive index $n(\theta, \omega)$ in these cases depends on the polarisation of the light. Specifically, it is influenced by the polarisation component of the light that is parallel to the optical axis. θ refers to the angle between the propagation direction of the wave and the optical axis of the crystal. For $\theta = 90°$, the respective refractive index n_e varies the most from the ordinary value n_o. The relation between the refractive index for an extraordinary wave and the angle θ describes an ellipse

$$\frac{1}{n^2(\theta, \omega)} = \frac{\cos^2\theta}{n_o^2(\omega)} + \frac{\sin^2\theta}{n_e^2(\omega)}. \tag{2.21}$$

For a beta barium borate (BBO) crystal the experimental refractive index dataset over its full transparency range ($0.188 - 5.2\,\mu\mathrm{m}$) is fitted by

$$n_o^2(\lambda) = 1 + \frac{0.90291 \cdot \lambda^2}{\lambda^2 - 0.003926} + \frac{0.83155 \cdot \lambda^2}{\lambda^2 - 0.018786} + \frac{0.76536 \cdot \lambda^2}{\lambda^2 - 60.01}, \tag{2.22}$$

$$n_e^2(\lambda) = 1 + \frac{1.151075 \cdot \lambda^2}{\lambda^2 - 0.007142} + \frac{0.21803 \cdot \lambda^2}{\lambda^2 - 0.02259} + \frac{0.656 \cdot \lambda^2}{\lambda^2 - 263} \tag{2.23}$$

with the wavelength λ in µm [27]. At a wavelength of 1039 nm, one obtains $n_o \approx 1.655$ and $n_e \approx 1.542$, whereas, at its second harmonic ($\lambda = 519.5\,\mathrm{nm}$), $n_o \approx 1.675$ and $n_e \approx 1.556$. Since the extraordinary refractive index is smaller than the ordinary one, BBO is called a negative uniaxial crystal.

There exist two different types of light interactions in a nonlinear medium: When two waves impinge on the medium, they exhibit either the same, referred to as Type I, or orthogonal polarisation, known as Type II. When a wave with a specific polarisation is focused on the medium, this results in a Type I interaction. For a Type I interaction the refractive index of an ordinary fundamental wave has to equal to the refractive index of an extraordinary second harmonic wave under a certain crystal angle θ. This can be visualised in index ellipsoid figures which are built up from spheres for the refractive index of the ordinary wave and ellipsoids for the refractive index of the extraordinary waves, both for the fundamental frequency ω and its overtone. For an uniaxial crystal, the index ellipsoid can be reduced to two dimensions.

Figure 2.4 shows a schematic index ellipsoid for BBO at $\lambda = 1039\,\mathrm{nm}$ though not to scale. An intersection in this case can only be found for an ordinary wave at the fundamental frequency and an extraordinary one at the second harmonic. This intersection occurs at the phase-matching angle θ of the crystal's optical axis with respect to the propagation direction. For BBO at $\lambda = 1039\,\mathrm{nm}$, it is $\theta = 23.0°$. With phase-matching in a birefringent crystal, one has laid the basis for observing an SHG signal. How to further fine tune the SHG process in order to increase its efficiency is treated in the following subsection.

[1], [22], [27]

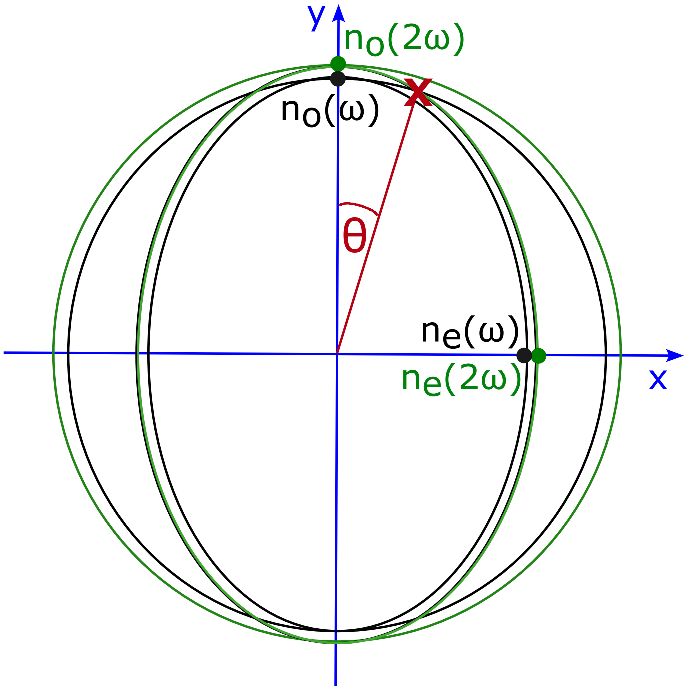

Figure 2.4: Index Ellipsoid for Type I phase-matching in a negative uniaxial crystal. The x-axis represents the extraordinary axis, while the y-axis represents the ordinary axis. According to Equation 2.21, the variation of the refractive index n with the polarisation angle for an extraordinary wave of fixed frequency forms an ellipse with half-axes n_o and n_e. For an ordinary wave of fixed frequency, n_o is independent of the polarisation angle, resulting in a circular shape. Here, the fundamental frequency ω is represent in black and its second harmonic 2ω in green. The ordinary wave at ω (black circle) intersects the extraordinary wave at 2ω (green ellipse) for the phase-matching angle θ (red).
Adapted from [22].

Efficiency of SHG

The efficiency of SHG is defined as the ratio of the SHG wave intensity $I(2\omega)$ to the fundamental wave intensity $I(\omega)$,

$$\eta_{\mathrm{SHG}} = \frac{I(2\omega)}{I(\omega)}. \tag{2.24}$$

The interpretation of the nonlinear part of the polarisation as a source as in Equation 2.15 means that this source term is proportional to the amplitude of the second-harmonic. Inserting the polarisation for an incident monochromatic wave, Equation 2.16, it results for the 2ω contribution in $I(2\omega) \propto (\chi^{(2)}\omega^2 I(\omega))^2$. Taking into account that one has a coherent superposition of atomic polarisations in the interaction volume of length L, $I(2\omega) \propto L^2$. Further rewriting $I(2\omega) = P/A$ as incident power P per cross-sectional area A of the interaction volume, one arrives at

$$\eta_{\mathrm{SHG}} \propto \left(\chi^{(2)}\omega^2\right)^2 \frac{L^2}{A} P. \tag{2.25}$$

To enhance the SHG efficiency, high laser intensities are advantageous which is where pulsed lasers come into play. [22]

2.2.2 Kerr effect

With high intensity light fields third order nonlinearities can not be neglected anymore. For media which exhibit a centrosymmetric structure, the leading nonlinearity is of third order,

$$P_{\mathrm{nl}} \approx \chi^{(3)} E^3. \tag{2.26}$$

They are called Kerr media. Their nonlinear polarisation component at the frequency ω can be seen as an incremental change in susceptibility therefore, also as an incremental change Δn for the refractive index,

$$\Delta n = \underbrace{\frac{3}{4n_0^2 c_0}\chi^{(3)}}_{n_2} \cdot I \tag{2.27}$$

with the light intensity $I = c_0 n \epsilon_0 / 2 \cdot |E(\omega)|^2$. n_2 is the Optical Kerr Coefficient which is a part of the total, now intensity dependent, refractive index $n(I)$

$$n(I) = n + n_2 I. \tag{2.28}$$

The optical Kerr effect can lead to several self-action effects important for nonlinear pulse compression: Self-focusing, self-trapping and laser beam breakup. For self-focusing, the nonlinear material acts as a positive lens since the high intensity center of the beam sees a larger refractive index than its periphery (assuming n_2 is positive). Balancing self-focusing and diffraction effects, light can propagate at a constant diameter which is called self-trapping. This occurs at the critical power for self-trapping

$$P_{\text{crit}} = \frac{\pi (0.61)^2 \lambda_0^2 \epsilon_0}{8 n_0 n_2} \tag{2.29}$$

with the vacuum wavelength λ_0 of the laser. For powers above P_{crit}, self-focusing occurs, and if $P \gg P_{\text{crit}}$ the beam will split into many components (due to imperfections of the laser wavefront), called laser beam break-up.
[22], [26], [28]

Self-focusing

Since self-focusing is a significant consequence of the Kerr effect, the following section presents the mathematical formulae relevant in practice. Using Fermat's principle as a starting point one can approximately deduce a characteristic self-focusing distance z_{sf} for the diffraction-free case with beam waist w_0 to

$$z_{\text{sf}} = \frac{2 n_0 w_0^2}{\lambda_0} \frac{1}{\sqrt{P / P_{\text{crit}}}}. \tag{2.30}$$

For a more general case with arbitrary power and beam-waist, the distance of the position $z(w_0)$ to the entry point into the nonlinear medium is introduces as z_{min}. With this and the beam waist at the entry point w, one has

$$z_{\text{sf}} = \frac{\frac{1}{2} k_0 w^2}{\sqrt{P / P_{\text{crit}} - 1} + 2 z_{\text{min}} / k_0 w_0^2} \tag{2.31}$$

where $k_0 = n_0\omega/c_0$ is the angular wave number. The above discussion is only valid for continuous wave lasers and has to be adapted for pulsed laser beams with a moving focus model: The self-focusing distance z_{sf} varies with the instantaneous input intensity of the pulse. Therefore, the focal point will sweep through the medium following the temporal evolution of the pulse.
[26]

Self-phase modulation

Self-phase modulation (SPM) is another consequence of the Kerr effect as a phase shift is induced by the beam travelling through the nonlinear medium. In the following, the medium is assumed to be thin in order to have no reshaping of the pulse and the response of the medium to be instantaneous. Focusing on the time-dependent component of the phase shift resulting from the optical Kerr coefficient n_2

$$\phi_{\mathrm{nl}}(t) = -n_2 I(t) k_0 L, \tag{2.32}$$

one observes that it is directly proportional to the length L of the nonlinear medium and the pulse intensity $I(t)$. Following the treatment of Section 2.1 about ultrashort laser pulses and introducing an instantaneous frequency as in Equation 2.9, the phase shift from the Kerr effect (Equation 2.32) introduces a frequency modulation, also known as chirp. Since the temporal and spectral pulse profiles are connected by the Fourier transform (Equation 2.4), this chirp commonly leads to spectral broadening of the pulse.
[22], [26]

2.3 Pulse compression

Ultrashort laser pulses may be further compressed in the time domain in several ways. The most straight-forward approach would use a linear dispersive element such as a grating or prism to remove the chirp of a pulse. If the pulse is already unchirped, meaning transform-limited, a phase modulator which keeps the pulse duration constant while introducing spectral broadening and a chirp might be applied. [22] For intense ultra short pulses it is favorable to make use of nonlinear dispersion based on the Kerr effect due to a higher power efficiency [19]. At laser powers in the same order of magnitude as P_{crit} (the critical power for self-trapping of a material) self-focusing sets an upper limit of the nonlinear medium's thickness. This in return limits the acquired nonlinear phase (see equation 2.32) which is the chirp of the pulse after having passed the medium. At this point the usefulness of a multi-pass approach through the nonlinear medium to step wise accumulate nonlinear phase is evident in the frame work of compressing intense ultrashort pulses. The next section presents the multi-pass approach for the case of a bulk nonlinear material in a simple geometry, the Herriott cell. Afterwards a brief overview of other techniques to compress intense ultrashort pulses is given.

2.3.1 Bulk multi-pass cell (MPC)

Bulk multi-pass cells have been successfully employed for ultrashort pulse compression within the peak power range from 10 MW to 1 GW. [19] A straightforward geometry for a multi-pass setup is the Herriott cell, shown in Figure 2.5. This configuration features two curved mirrors with identical radii of curvature, denoted as CM_1 and CM_2. The mirrors face each other with a nonlinear bulk material positioned between them. A laser beam, introduced at a slight angle to the central axis connecting the mirrors, can be confined within this setup.

The laser beam can be coupled in and out of the cell through various methods, such as using two small scraper mirrors, SM_1 and SM_2. Figure 2.5 is a schematic representation and not to scale; in practice, the nonlinear medium would typically be much smaller than the curved mirrors, and the laser paths would be tightly focused in the center.

Beam propagation in a Herriott cell

In a Herriott cell, transverse eigenmodes exist, and the cell is designed to preserve the Gaussian beam q-parameter. As such, it can be treated with the same formalism as an optical cavity. Here, only the q-parameter of the eigenmode is presented; for details on deviations, refer to [10], [20] and [29]. The q-parameter is

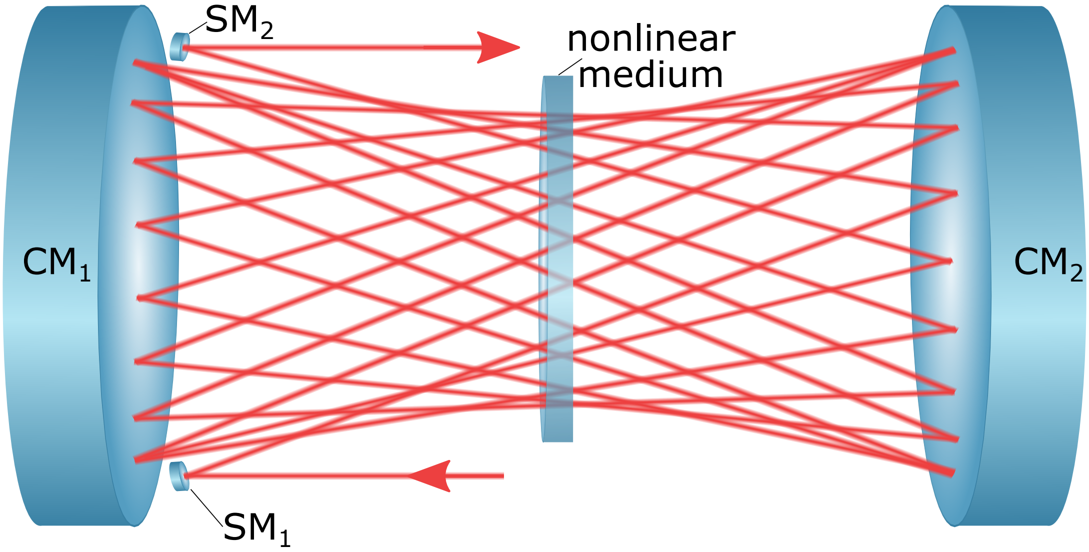

Figure 2.5: Schematic of a Herriott cell geometry adapted for the use as a multi-pass cell. Two curved mirrors CM$_1$ and CM$_2$ face each other with a nonlinear medium in between. The laser beam (red) is trapped cavity-like in the cell. It is coupled in and out with scraper mirrors SM$_1$ and SM$_2$. Adapted from [10].

fully defined by the radii of curvature of the mirrors R and the length of the cell L, e.g. the mirror distance as

$$q = -\frac{R}{2}\sqrt{C\,(C-2)}. \tag{2.33}$$

with the ratio $C = L/R$. The cell length has to fulfill $0 < L < 2R$ in order to be in the stable cavity range. [19] The q-parameter allows the prediction of curvature and beam size. Especially the focal spot radius w_0 and the spot radius at the mirror position w_m are of practical importance

$$w_0^2 = \frac{R\lambda}{2\pi}\sqrt{C\,(2-C)}, \tag{2.34}$$

$$w_m^2 = \frac{R\lambda}{\pi}\sqrt{\frac{C}{2-C}}. \tag{2.35}$$

[19]

Laser spot pattern

In this section the laser spot pattern on the first MPC mirror (the mirror where the beam is in- and outcoupled, CM_1 in Figure 2.5) is detailed. This laser spot pattern illustrated in Figure 2.6 is characterised by several key quantities:

- n number of round trips: One round trip starts at the first mirror, includes a first pass through the nonlinear element, then a reflection at the second mirror, a second pass through the nonlinear element, and ends back at the first mirror.
- ϕ angle of spot displacement: The angle by which the laser spot position on one mirror changes after one round trip is represented by ϕ. Figure 2.6 a) illustrates how the laser spot with coordinates (x_n, y_n) advances by ϕ after each round trip.
- m number of semicircles: This is the number of semicircles the spots span on the first mirror from incoupling to outcoupling. In our Herriott cell design, where outcoupling occurs on the opposite side of the mirror from incoupling, m must be an odd number.

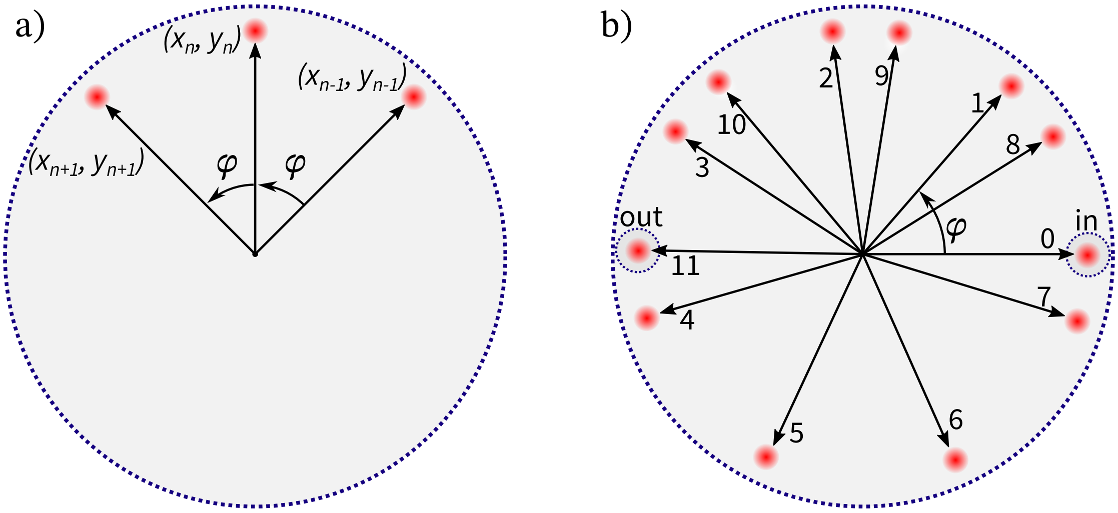

Figure 2.6: Schematic laser spot pattern on the first MPC mirror a) One round trip $\Delta n = 1$ advances the spot (x_n, y_n) by an angle of ϕ. b) Complete spot pattern for $n = 11$ and $m = 3$, which implies $\phi = 49.1°$. Figure from [10].

These quantities are related by $\phi = m\pi(n-1)/n$ which stems from the q-parameter preservation [19]. Figure 2.6 b) shows the case of 22 passes ($n = 11$) with a choice of $m = 3$, resulting in $\phi = 49.1°$.

Building on the previous subsection, theory also establishes a relationship between the angle ϕ and the ratio,$C = L/R$, of cell length to the mirror's radii of curvature

$$C = 1 - \cos(\phi/2) \tag{2.36}$$

[29]. Therefore, when assuming a fixed radius of curvature, the specific choice of a combination of n and m directly determines the required cell length L.

Nonlinear phase accumulation

Building on the geometric analysis of the Herriott cell, the following section delves deeper into the nonlinear effects and their stepwise accumulation. Although nonlinearity has an impact on the previously deduced optical mode, J. Schulte and colleagues have experimentally demonstrated that the q-parameter is barely influenced by the input power [30]. Therefore, also valid for our experiment, the nonlinear effects on the q-parameter are assumed to be negligible.

To quantify spectral broadening, the B-integral is a useful measure. Here it is defined as the accumulated on-axis nonlinear phase

$$B := \frac{2\pi}{\lambda} \int n_2 I_p(z) dz \tag{2.37}$$

where $I_p(z)$ represents the laser peak intensity along the optical axis z [19]. For a Gaussian beam with Rayleigh length z_R and a nonlinear medium with a length less than the Rayleigh length ($L < z_R$), the laser intensity varies by only a few percent within the medium. Therefore, Equation 2.37 can be approximated as

$$B_{\text{pass}} \approx \frac{4n_2 P_p}{\lambda\pi} \frac{L}{w_0^2} \cdot \pi \tag{2.38}$$

with the pulse peak power P_p. It is important to note that a narrower waist will not necessarily lead to an increased B-integral if $L < z_R$ is not met, as the pulse intensity will decrease significantly over the crystal length. The B-integral has been named B_{pass} to emphasis that only one pass of the nonlinear medium has been considered until here. "The B-integral per pass within an MPC containing a bulk plate as nonlinear medium is usually kept small (e.g., below $\pi/5$)." [19] The B-integral accumulates with each pass, so the total B-integral after n round trips, denoted as B_n, is $B_n = 2nB_{\text{pass}}$. For a Gaussian beam, the B-integral is directly linked to the spectral broadening factor

$$b_n = \frac{\Delta\omega_{\text{out}}}{\Delta\omega_{\text{in}}} = \sqrt{1 + \frac{B_n^2}{3\sqrt{3}}} \tag{2.39}$$

which gives the ratio between in- $\Delta\omega_{\text{in}}$ and outgoing bandwidth $\Delta\omega_{\text{out}}$ of the laser pulse.

Key parameters

This section provides a brief overview of the key parameters of the MPC that influence its pulse compression, following closely the description in [20]. These parameters must be tailored to the application and pulse specifics.

- Nonlinear medium: The pulse's peak power and the desired spectral broadening factor form the basis for selecting a nonlinear medium with an appropriate optical Kerr coefficient n_2. A key advantage of the MPC is its ability to allow the pulse's peak power to exceed the critical power for self-focusing of the nonlinear medium [31]. Fused silica is a commonly chosen medium [19], [30].

- Curved mirrors: The radii of curvature R of the mirrors set the maximum cell length and must balance compactness with lower peak intensities at the mirrors' focus. The mirrors' circumferences must accommodate the spot pattern with sufficient spacing.

- Inter-mirror distance L: With fixed radii of curvature, the inter-mirror distance determines according to Equation 2.34 the focal spot radius which in turn influences the B-Integral (Equation 2.38). Additionally, it affects the angle ϕ of spot displacement on one mirror per round trip (Equation 2.36), establishing a set number of spots per circle. Along with the outcoupling requirement of an odd number of semicircles m, these factors narrow down the possible number of round trips n. To sum up, the inter-mirror distance determines the spectral broadening factor within a narrow margin [2]. For $R = 250\,\text{mm}$, these dependencies on the cell length are illustrated in Figure 2.7.

- Dispersion compensation: The nonlinear element introduces dispersion that must be managed [31]. If dispersion is too high, the pulse's peak power will diminish pass by pass, reducing the B-integral per pass nonlinearly. To counteract this undesired effect, chirped MPC mirrors can be used. Conversely,

---

[2] assuming a fixed pulse peak power, nonlinear element, cell length and radii of curvature

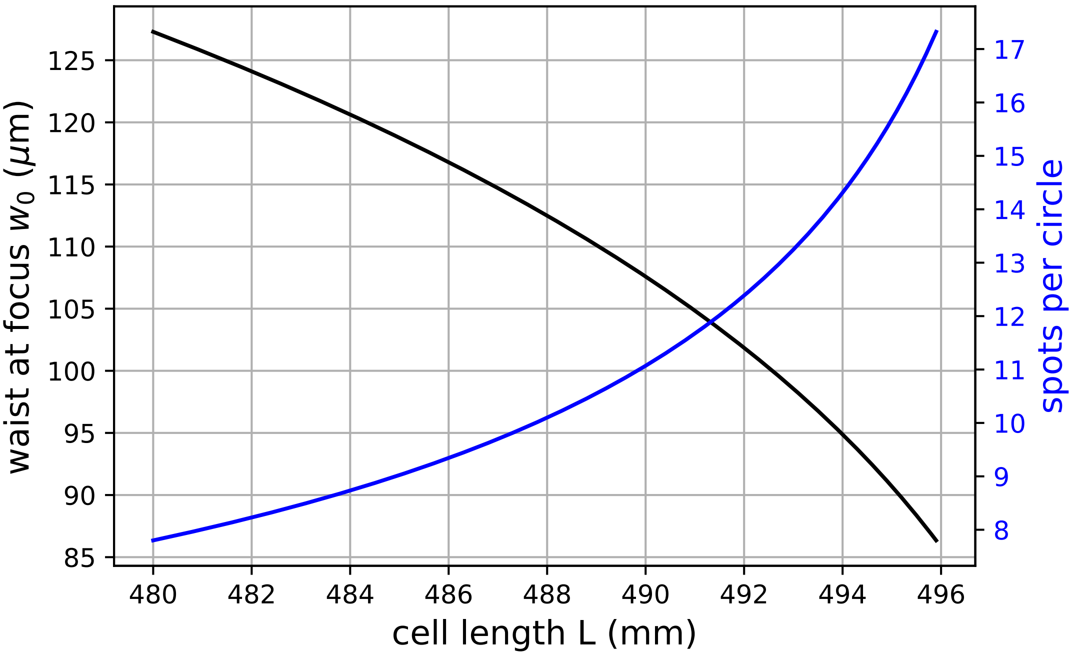

Figure 2.7: Dependencies on the MPC cell length for a radius of curvature $R = 250\,\text{mm}$. The waist at the focus is dependent on the cell length from Equation 2.34 and the spots per circle from Equation 2.36. There is a stability edge at $L = 500\,\text{mm}$.

if dispersion per pass is fully compensated, thus compressing the pulse temporally, the pulse's peak power would increase with each pass. Again, this is an undesired effect as modulation instabilities would occur. The goal is to partially compensate for the nonlinear element's dispersion. Therefore, a post-compression stage must be added after the MPC to compensate for the remaining dispersion and attain the Fourier-transform limit for the pulse duration [31].

2.3.2 Other techniques

As previously detailed, an MPC containing a bulk nonlinear medium serves as a suitable tool to compress ultrahort pulses with peak powers that exceed the medium's critical power of self-focusing. Another variant of the MPC is the gas-filled MPC, which employs a noble gas filling instead of a bulk nonlinear element. Gas-filled MPCs are designed for even higher peak powers, ranging from approximately 10 MW to around 80 GW [19]. This significant power handling capability is attributed to gases having a three orders of magnitude higher critical self-focusing threshold compared to bulk materials [30]. Moreover, gas-filled MPCs offer several advantages, reduced losses due to the absence of optical interfaces, no risk for damage to the nonlinear medium, and broad transparency windows across the spectrum [19].

Stepping away from MPCs, waveguides represent the standard pulse compression scheme for ultrashort pulses. Like MPCs, waveguides can be categorised into solid-based waveguides, primarily fused silica fibers, and gas-filled waveguides. However, fused silica fibers are constrained to peak powers of around 4 MW due to self-focusing effects. On the other hand, gas-filled waveguides can accommodate peak energies of GW and beyond for pulses lasting a few hundred femtoseconds. This energy range presents a gap where MPCs offer a valuable solution.

2.4 Pulse characterisation

Measuring ultrashort pulses presents a significant challenge due to the absence of electronic devices for direct measurement. For example, the temporal resolution of PIN photodiodes is limited to 20 ps, and streak cameras only achieve a resolution of 400 fs. For shorter pulses, it is impossible to reference the pulse with an external electronic reference; thus, the pulse itself can take on the role of a reference. An intuitive approach would be measuring the intensity $I(t,\tau) = c_0\epsilon_0[E(t)+E(t+\tau)]^2$ of a pulse $E(t)$ and its by the time τ delayed copy with a detector with integration time T,

$$S_D =< I(t,\tau) >= \frac{1}{2T}\int_{-T}^{+T} I(t,\tau)dt. \tag{2.40}$$

The signal S_D of the detector is obviously independent of τ and the pulse shape for $T >> \tau$ [1]. Also for a very fast detector resolving $I(\tau)$, only spectral not temporal information can be retrieved with a Fourier transform [32]. Therefore, another step is necessary, which is introducing a nonlinear interaction before the detection. The most obvious choice is SHG as the efficiency of nonlinear effects rapidly decreases with higher orders. [1]
In the following section, the case of SHG in an uniaxial birefringent crystal is implied. Other techniques are discussed in the section thereafter.

2.4.1 Autocorrelation

One can transfer the following principles for monochromatic waves with Fourier analysis to more complex pulse shapes. The starting point is the polarisation of a nonlinear medium in the case of a monochromatic wave for SHG, Equation 2.16. In case only the second harmonic is filtered, one can write the signal electric field strength of the second harmonic as

$$E_{\mathrm{sig}}(t,\tau) \propto E(t)E(t-\tau). \tag{2.41}$$

Inserting the signal intensity $I_{\mathrm{sig}}(t,\tau)$ into the expression for the detector signal (Equation 2.40) gives the mathematical expression of a convolution

$$S_D \propto \int I(t)I(t-\tau)dt. \tag{2.42}$$

For a known pulse shape, the autocorrelation can thus provide information about the pulse duration τ_p. As demonstrated by R. Trebino, for more complex and unknown pulse shapes, the information retrievable from the autocorrelation is very limited.
[33]

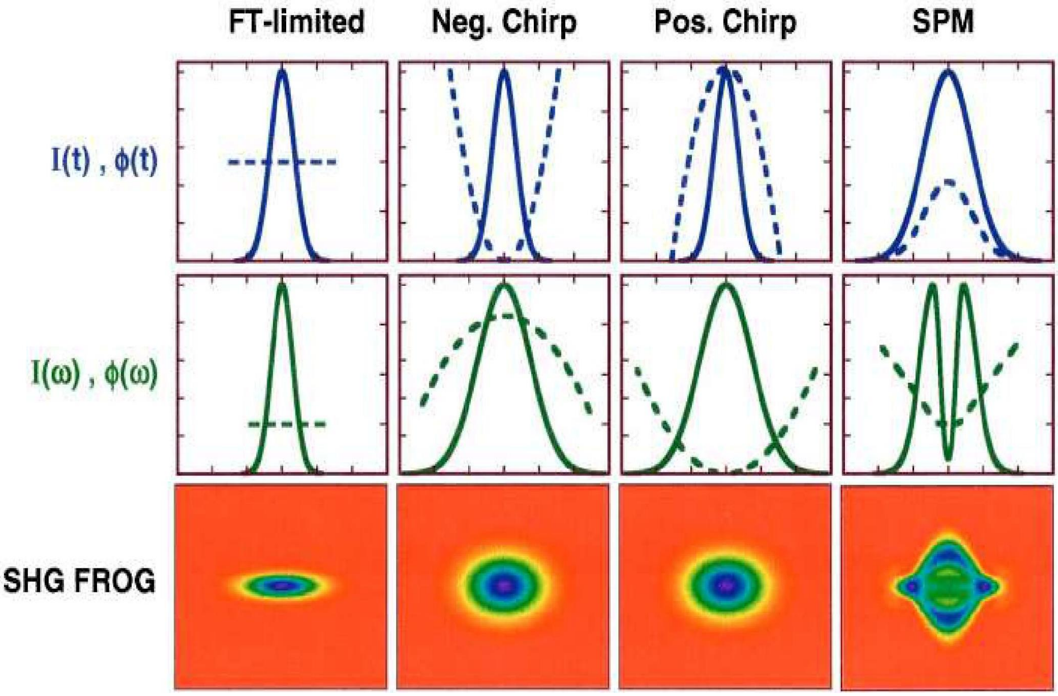

Figure 2.8: Typical basic pulse shapes and their computed SHG FROG traces. The upper panels depict the intensity I (blue line) and the phase Φ (dashed blue line) as functions of time t. The middle row of panels display intensity I (green line) and the phase Φ (dashed green line) in the spectral domain ω. The SHG FROG traces plot time t on the x-axis versus frequency ω on the y-axis. The associated intensities are plotted on a colour scale from orange (low) to purple (high). Figure from [34].

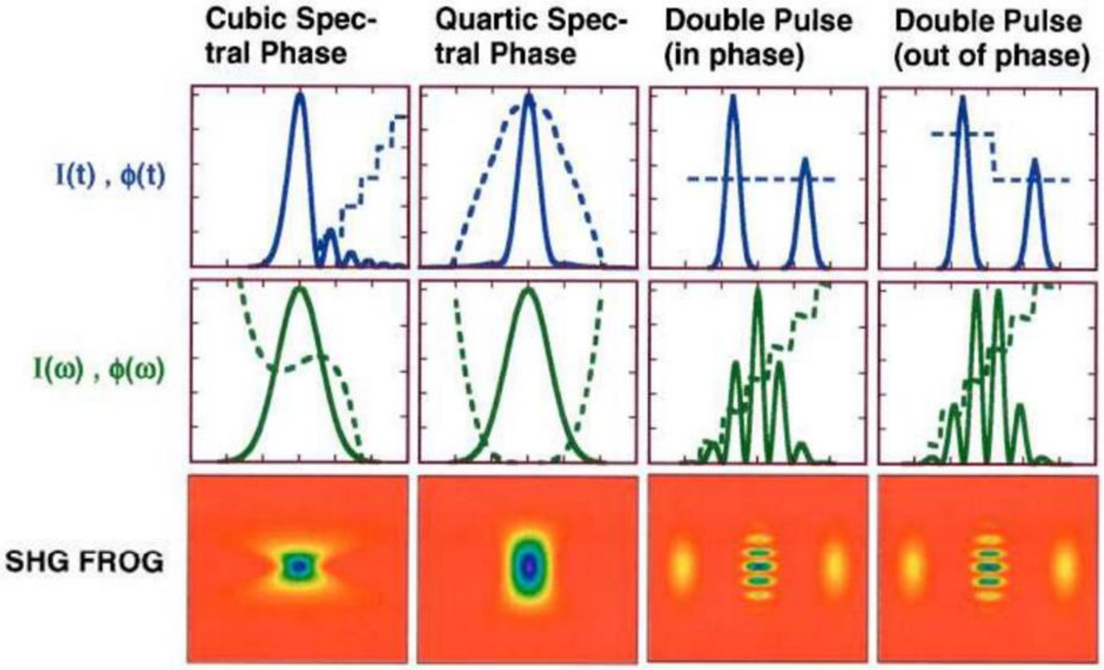

Figure 2.9: Typical pulse shapes and their computed SHG FROG traces. The upper panels depict the intensity I (blue line) and the phase Φ (dashed blue line) as functions of time t. The middle row of panels display intensity I (green line) and the phase Φ (dashed green line) in the spectral domain ω. The SHG FROG traces plot time t on the x-axis versus frequency ω on the y-axis. The associated intensities are plotted on a colour scale from orange (low) to purple (high). Figure from [34].

2.4.2 Frequency Resolved Optical Gating (FROG)

Resolving the autocorrelation signal spectrally can bridge the gap to obtain more information about (complex) ultrafast pulses. This method of Frequency Resolved Optical Gating (FROG) has been first detailed by Rick Trebino in 1993 [34]. For each delay τ, a spectrum is plotted along the y-axis, with intensity values represented on a colour scale. This plot, termed a FROG trace, is given by

$$I_{\text{FROG}}(\omega, \tau) = |\int_{-\infty}^{\infty} E_{\text{sig}}(t, \tau) \exp(-i\omega t) dt|^2. \tag{2.43}$$

From a FROG trace, one can retrieve the pulses electric field $E(t)$.

Typical pulse shapes and their computed FROG traces

For an intuition how the SHG FROG traces are linked to the pulse shape, Figure 2.8 shows the computed FROG traces associated with the typical basic pulse shapes, namely a Fourier-Transform limited Gaussian, a Gaussian with negative (positive) chirp and a self-phase modulated one. Figure 2.9 introduces slightly more complex pulse shapes, specifically including cubic and quartic spectral phases, as well as double pulses (in and out of phase). It should be noted that the SHG FROG traces are by construction symmetrical with respect to zero delay.
[34]

Advantages

FROG offers several advantages, including its versatility across a wide range of wavelengths, pulse durations, and complexities, along with the simplicity of its apparatus. Moreover, it is a robust and accurate method, resilient to noise, and provides feedback on the quality of the retrieval, helping to identify and address systematic errors. The last point is a probabilistic argument resulting from the over definition of the FROG trace. If one measures the number of N data points both spectrally and with respect to delay, in total N^2 data points are available to retrieve $2N$ values, the electric field strength and its phase for each wavelength. This leads to the retrieval problem treated in the next paragraph. [34], [35]

Pulse retrieval from the FROG trace

The initial proposed retrieval by R. Trebino [34] is the Principal Component Generalised Projections Algorithm (PCGPA) which uses two sets of solutions and projects in each step to the closest point in the other set. The first set of solutions solves Equation 2.41, whereas the second is a solution to Equation 2.43. As these two sets of solutions for FROG are not convex, the projection is not necessarily unique. Further, the temporal resolution is limited by the spectral bandwidth experimentally obtainable, since a quadratic $N \times N$ FROG trace is required.
These difficulties can be overcome by applying the extended Ptychographical Iterative Engine (ePIE) which is an algorithm from ptychography demonstrated by Sidorenko and coworkers in 2016 [36]. It offers significantly faster retrieval, increased robustness to noise, and enables retrieval from partial spectrograms, thereby reducing experimental acquisition time [36]. Therefore, in this thesis only ePIE will be further detailed and used.
In a nutshell, ePIE starts with an initial guess $E^{(0)}(t)$ for the electric field of the pulse. Then, based on a comparison to the measured trace $I_{\text{FROG}}(\omega, t)$ this guess will be iteratively improved until certain stopping criteria are fulfilled.
A stopping criterion can be defined using the FROG error G, which represents the root mean square deviation of the (as yet unnormalised) FROG intensity after the k-th iteration $I^{(k)}_{\text{FROG}}$,

$$G = \sqrt{\frac{1}{N^2} \sum_{i,j=1}^{N} |I_{\text{FROG}}(\omega_i, \tau_j) - \alpha I^{(k)}_{\text{FROG}}(\omega_i, \tau_j)|^2}. \tag{2.44}$$

Here, $I_{\text{FROG}}(\omega_i, \tau_j)$ represents the normalised measured trace for each data point with indexes i, j from 1 to N. α is a real-valued parameter that minimises the FROG error to ensure renormalisation. For noise-free data, the limits of the machine error result in $G \sim 10^{-7}$, in experiments with $N = 128$ for SHG typically $G < 0.5\%$ [34]. In practice, the minimisation of the FROG error is limited by noise and experimental deviation from a physically valid trace (e.g. distortions, systematic errors, stray light) [35]. Further stopping criteria may include a maximum number of iterations, maximum iteration time and a stagnation count [37].

For a more detailed understanding of the iterative process aimed at refining the guess for the electric field, refer to Figure 2.10. In the upper right corner the initial guess, based on the retrieval amplitude N-grid algorithm (RANA), is depicted. Subsequently, an internal loop proceeds over the delay steps, labelled $j = \tau \cdot \Delta t$, in a random order $s(j)$. It is worth highlighting that this internal loop is the heart of the algorithm which will be elucidated in the following.
For each delay step, the signal intensity $\Psi_{s(j)}(t)$ with the current guess is computed in the time domain and Fourier transformed to the spectral domain. Then, the signal intensity is modified to $\Psi`_{s(j)}(\omega)$ including the measured trace $I_{s(j)}(\omega)$ and inversely transformed to the time domain. Following that, the crucial step is creating a new guess for the electric field of the next delay step $s(j)+1$. This is done by modifying $E_{s(j)}$ according to the difference of the modified signal intensity $\Psi`_{s(j)}(t)$ and the original one, $\Psi_{s(j)}(t)$. For faster convergence, a random update strength α between 0.1 and 0.5 is introduced.
The new guesses for every delay step add up to a the electric field guess of the next iteration step i, $E^{(i)}(t)$. Optionally, this new electric field guess can be modified with an independently measured spectrum $I_{\text{spec}}(\omega)$ according to

$$E'^{(i)}(\omega) = E^{(i)}(\omega) + \beta \left(\frac{\sqrt{I_{\text{spec}}(\omega)} E^{(i)}(\omega)}{|E^{(i)}(\omega)|} - E^{(i)}(\omega) \right) \tag{2.45}$$

with a random update strength β.[3]
[36]

Accuracy of the retrieved FROG trace Ambiguities of the SHG FROG method are the direction of time and a global phase of the pulse [36]. As experimental data usually contains noise and systematic errors, it is generally not among the set of physically valid FROG traces. Therefore, it will converge to the nearest physically valid trace which is not necessarily equivalent to the trace of an ideal

---

[3] This way of updating the electric field guess with an independently measured spectrum is my version.

measurement. Thus, a noise correction and symmetrisation with respect to zero delay prior to the retrieval process is beneficial [21]. A quantitative measure for the convergence of the retrieval algorithm, the FROG error, Equation 2.44, has already been introduced. However, the FROG error can only be seen as an indicator for the accuracy and necessitating an additional visual comparison between the experimentally obtained and the retrieved trace [35]. A consistency check of the FROG trace can be done by computing the frequency marginal $M(\omega)$

$$M(\omega) = \int_{-\infty}^{\infty} I_{\text{FROG}}(\omega, \tau) d\tau \tag{2.46}$$

which should have a functional form identical to the autoconvolution (denoted by an asterisk) of the pulse spectrum $I(\omega - \omega_0)$ centered around the carrier frequency ω_0,

$$M_{\text{SHG}}(\omega - 2\omega_0) = I(\omega - \omega_0) * I(\omega - \omega_0). \tag{2.47}$$

[35]

2.4.3 Other techniques

The preceding section on FROG implied the case of SHG in an uniaxial birefringent crystal. In the following, first alternative FROG implementations are outlined. Secondly, alternatives to FROG itself are presented.

A variation of SHG FROG which is easier to align is the interferometric Frequency Resolved Optical Gating (iFROG) [21]. In this setup, both the pulse and its delayed counterpart are directed onto the nonlinear crystal along the same path, rather than being separately focused onto distinct spots within the crystal. Consequently, the electric field strength of the signal results from the summation of the complex electric fields, as opposed to the summation of their intensities as in previous configurations. With the representation of the complex electric field as a real field envelope $A(t)$ and a phase contribution of the carrier frequency ω_c as in

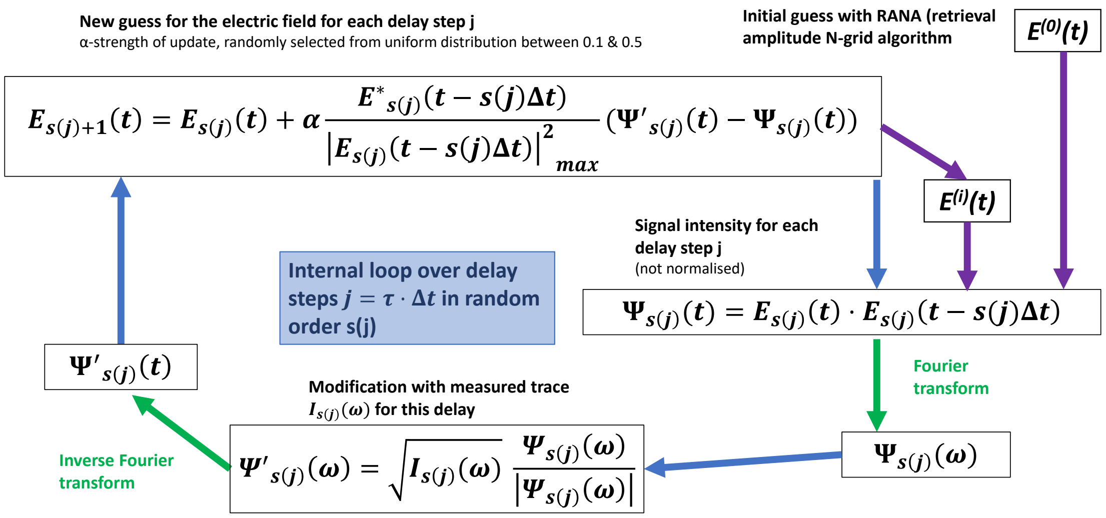

Figure 2.10: Illustration of the internal loop in the ePIE retrieval algorithm. The loop starts in the upper right corner with the initial guess and iterates over all delay steps j. Upon completion, a new electric field guess $E^{(i)}(t)$ is obtained, serving as the starting point for the next iteration of the loop. Equations from [36], design adapted from [21].

Equation 2.8 where $\Phi(t) = \Phi(t-\tau)$ is assumed, one gets

$$E_{\text{sig,iFROG}}(t,\tau) \propto (E(t) + E(t-\tau))^2 \propto (A(t) + A(t-\tau)e^{-i\omega_c\tau})^2. \tag{2.48}$$

The phase difference $\omega_c\tau$ overlays an interferometric pattern to the previously treated noncollinear FROG traces. A modified ePIE retrieval algorithm is available for the interferometric case, developped by S. Kokh [21]. The downside to an easier alignment are longer data acquisition times to resolve the interference pattern.
[38]
A compact implementation of SHG FROG is called GRENOUILLE which stands for grating-eliminated no-nonsense observation of ultra-fast laser-light E-fields. In the GRENOUILLE set-up, the split-and-delay line is replaced by a Fresnel biprism and the group velocity mismatch in a thick nonlinear crystal takes the function of a spectrometer. Contrarily, in the standard SHG FROG a thin crstal is required since phasematching should be fulfilled for the complete pulse spectrum. However, GRENOUILLE comes with drawbacks, including reduced spectral resolution and potential pulse distortion caused by group velocity dispersion, particularly for ultrashort pulses. [39]
Another version, not needing a split-and-delay line, is called a single-shot set-up. The idea is to mix two pulses at an angle in the nonlinear crystal obtaining a range of delays along the crystal plane [40], [41].
Instead of SHG, one can also use third harmonic generation (THG). Generally this results in a weaker signal, but it removes the time ambiguity which is present in an SHG FROG trace. There are various THG FROG beam geometries which each have their advantages and disadvantages depending on the pulse specifications. [34]
R. Trebino and colleagues stated in 2020: "FROG was the first and remains the most powerful and popular pulse-measurement technique" [42]. However, for very weak pulses nonlinear effects might not be measurable anymore. Moreover, with very complicated pulses a FROG retrieval might require extensive computing resources. In these cases, spectral interferometry (SI) and its self-referenced version spectral phase interferometry for direct electric-field reconstruction (SPIDER) be-

come of interest. For SI, a completely known reference pulse which contains the spectrum of the unknown pulse is required. The basic idea is to overlay the reference and unknown pulse in a beam splitter and detect the spectrum. The unknown pulse can be reconstructed easily from the resulting spectral interference pattern. SPIDER does not need a known reference pulse, instead uses a frequency shifted version of the unknown pulse. For SPIDER, a careful calibration is required and stability proofs to be challenging.
[42]

3 Experimental Set-Up

This chapter details, in a first section, how the laser pulse is prepared before it enters the MPC. Up to this point, the laser pulses have been directed either to the MPC or to the XUV generation set-up. The desired goal of utilising the in the MPC compressed pulses for XUV generation has yet to be realised. The second section is dedicated to the MPC itself, including mode-matching and post-compression set-ups. The third sections explains the FROG set-up detailing how a variably delayed pulse copy is generated, the SHG on a removable breadboard and the spectrometer recording the FROG traces.

3.1 Laser pulse preparation for XUV generation

This description follows J.-H. Oelmann [10] and J. Nauta [11].
Figure 3.1 shows a schematic overview: The starting point is a commercial frequency comb (Menlo Systems, FC1000-250) with a 14 nm FWHM spectral bandwidth centered around 1039 nm. The pulse train with up to 12 W of average power is composed of 24 ps long pulses with a repetition rate $f_{\mathrm{rep}} = 100\,\mathrm{MHz}$ that can be adjusted by 1%. The repetition rate can be stabilized to a fractional uncertainty of 10^{-12} within one second.
In the next step, the near-infrared frequency comb is amplified using the concept of chirped-pulse amplification. This is realised in a rod-type large-mode-area (LMA) Yb-doped fiber (aeroGAIN rod module 2.0 PM85, NKT photonics) which is backward pumped with continuous wave light at 976 nm of a fiber-coupled laser diode with 250 W power (D4F2S22-976.3-250C-IS58.1, DILAS) coupled in with an off-axis parabolic mirror (OAP). The comb laser is protected from backward reflections by two high power Faraday isolators (ISO) (PAVOS Ultra-05–I-1015-1065, Soliton and HPKT-I-1042, IPOptica). Two half-waveplates (WPH10M-1030,

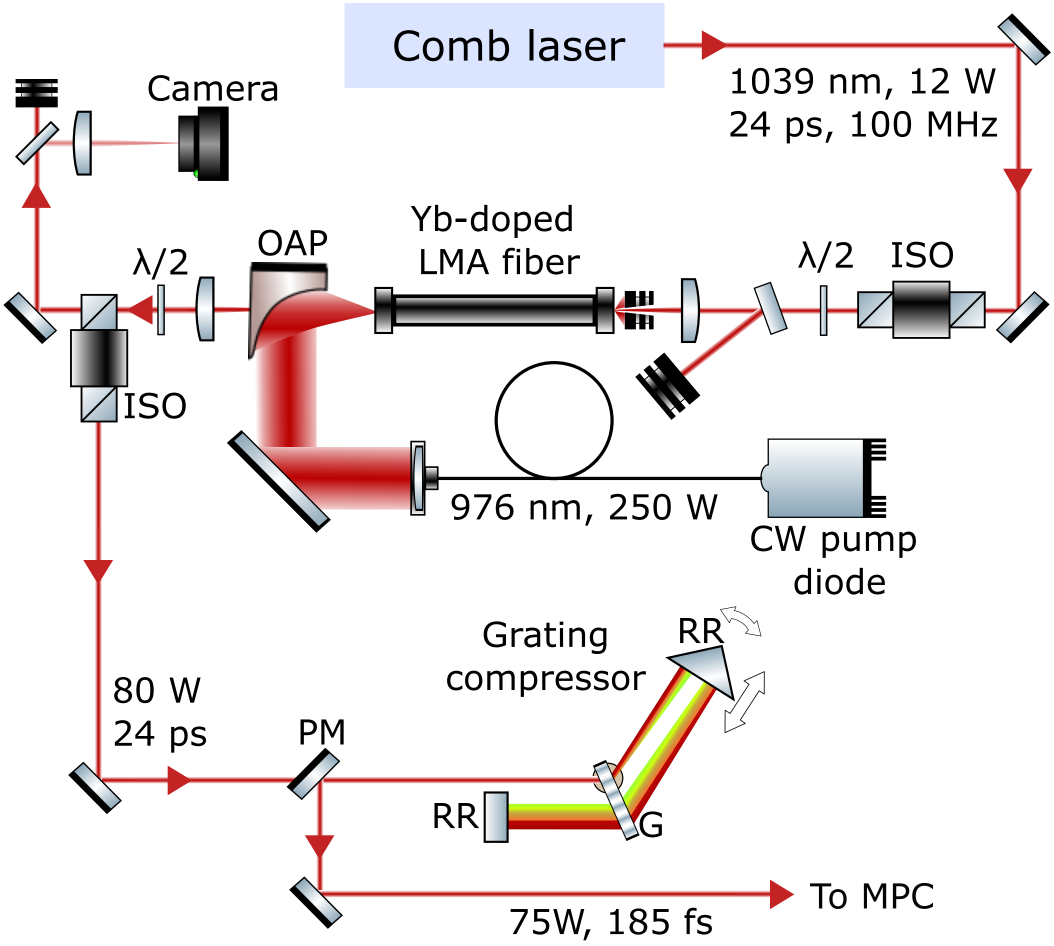

Figure 3.1: Schematic overview of the laser system before the MPC and subsequent HHG generation stage. The NIR comb laser is amplified in a Yb-doped large-mode-area (LMA) fiber which is diode-pumped via an off-axis parabolic mirror (OAP). Two Faraday isolators (ISO) prevent backward coupling. A grating compressor consisting of a pair of retroreflectors (RR) and a grating (G) removes the pulse's chirp. The 185 fs long pulse with 75 W is reflected on the picking mirror (PM) with a vertical offset towards the MPC. Figure from [10].

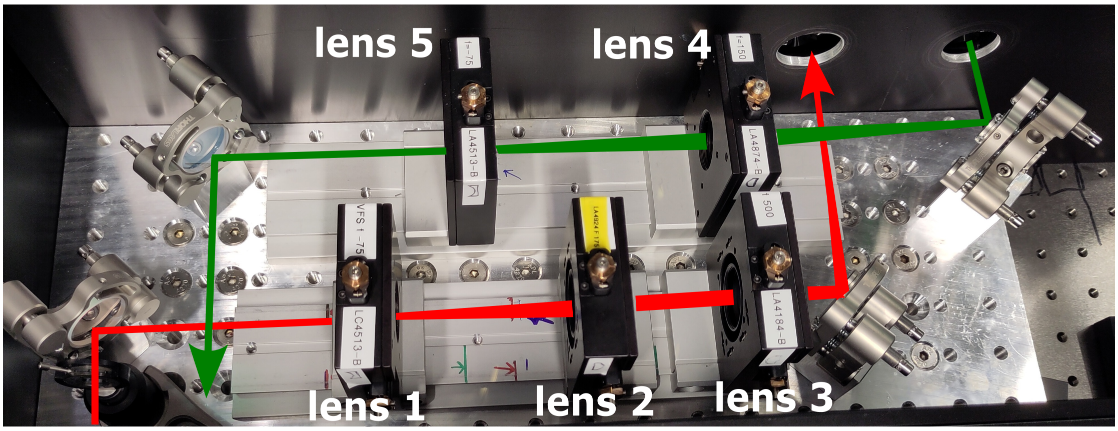

Figure 3.2: Mode-matching telescope for the MPC. The incoming beam (red) is attributed a specific waist by the combination of a diverging lens (lens 1, $f = -75\,\mathrm{mm}$) and a collimating lens (lens 2, $f = 175\,\mathrm{mm}$). Lens 3 ($f = 500\,\mathrm{mm}$) tunes the focus position. The outgoing beam (green) is collimated by lens 4 ($f = 150\,\mathrm{mm}$) and lens 5 ($f = -75\,\mathrm{mm}$).

Thorlabs), labelled $\lambda/2$, are used to adjust the polarisation before the fiber and second isolator. A grating compressor compresses the pulses from 24 ps to ~ 200 fs. This is achieved by a grating (1158 2818 6.35 H, Gitterwerk GmbH), labelled G, fanning out the different frequency components in space resulting in them having a slightly different paths length between a pair of retroreflectors (RR). A picking mirror (PM) with a vertical offset reflects the pulse to an MPC. In the MPC, the Fourier transform-limited pulses from the grating compressor are spectrally broadened before undergoing temporal compression to reach the reduced Fourier transform limit. Subsequently, they are directed to the HHG cavity for XUV generation.

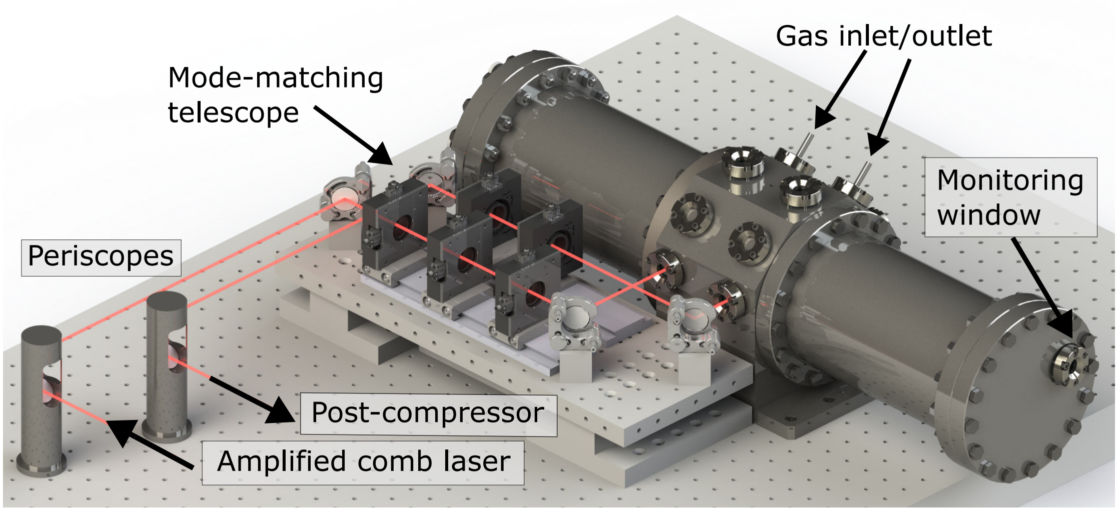

Figure 3.3: Design of the in- and outcoupling to the MPC. The amplified near-infrared frequency comb laser is guided by a periscope from 81 mm to 123.3 mm beam height. A mode-matching telescope focuses the beam in the center of the MPC to a desired waist. The MPC itself can be pressurised through the gas in- and outlet and observed from the outside through a monitoring window. After exciting the MPC, the beam is collimated and sent to a post-compressor consisting of chirped mirrors. Another periscope reduces the beam height to its original value. It can be placed either before (as in the figure) or after a post-compressor. Adapted from [20].

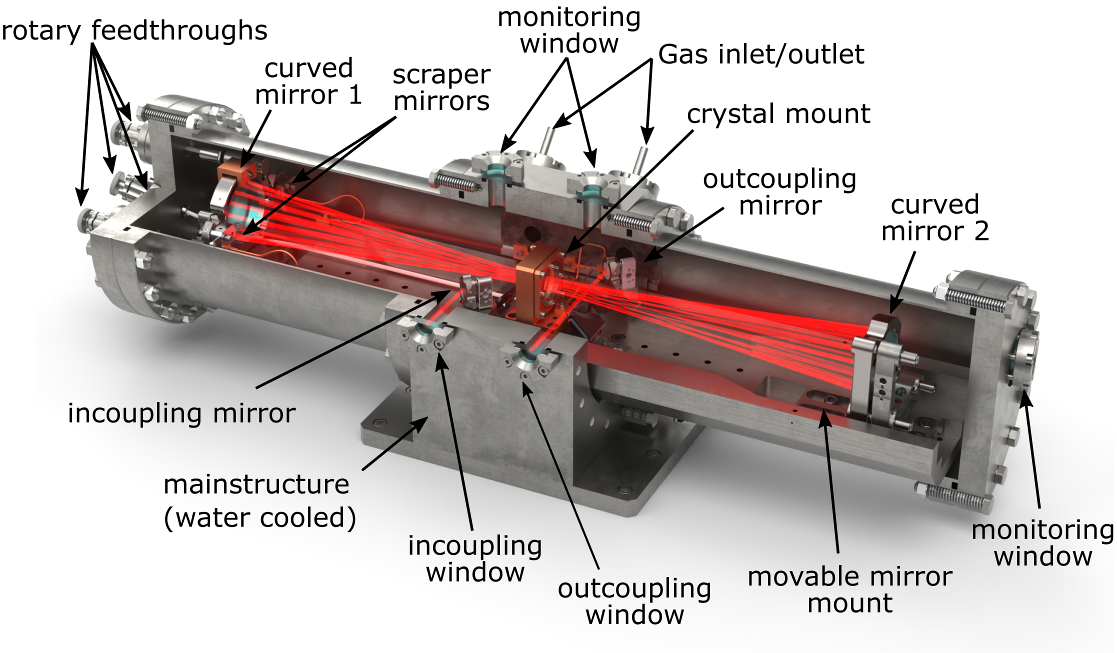

Figure 3.4: Sectional view of the MPC design with exemplary beam path. The cell can be pressurised and vacuumised using the gas in- and outlet. Its design allows for a closed operation with rotary feedthroughs and monitoring windows. The beam enters through the incoupling window onto the incoupling mirror and scraper mirror. Then, it propagates back and forth between curved mirror 1 and 2, each time passing the crystal until outcoupled by the second scraper mirror. It leaves the cell via the outcoupling mirror through the outcoupling window. Adapted from [10].

3.2 MPC

As seen in Figure 3.3 the MPC is inside an air-tight pipe which can be pressurised and vacuumised through gas inlets. Firstly, the beam height of the amplified and compressed comb laser is increased from 81 mm to 123.3 mm. Secondly, the beam is mode-matched in a telescope as shown in Figure 3.2: A diverging lens (lens 1, LC4513-B $f = -75\,\mathrm{mm}$, Thorlabs) in combination with a collimating lens (lens 2, LA4924-B $f = 175\,\mathrm{mm}$, Thorlabs) determine the beam waist. For a slight change in beam waist a change in focal length from $f = 150\,\mathrm{mm}$ to $f = 200\,\mathrm{mm}$ can be employed. A third lens (LA4184-B $f = 500\,\mathrm{mm}$, Thorlabs) is used to tune the focus position. The lenses are mounted in adjustable mounts (ST1XY-A/M, Thorlabs) on a rail.

Thirdly, the beam is guided in the MPC by a mirror (Turning mirror 45°, 141501, Layertec) through an incoupling window (AR-coated fused silica, ⌀25 mm, 111042, Layertec).

The interior design of the MPC is visualised in Figure 3.4: A mirror (BB07-E03, Thorlabs) on a 2-axis kinematic mount (POLARIS-K19S4, Thorlabs) guides the beam onto the incoupling scraper mirror (⌀6.35 mm, 107290, Layertec) where Figure 3.5 allows a closer view. The scraper mirrors are glued on aluminium arms, which can be adjusted in length and turned using an inlet into a mirror mount (Polaris-K05, Thorlabs). The incoupling scraper reflects the beam through the crystal mount onto the second curved mirror ($R = 250\,\mathrm{mm}$, ⌀50 mm, $\mathrm{GDD} = -200\,\mathrm{fs}^2$ custom-made, Layertec). The beam propagates in between the curved mirrors until it is outcoupled by an identical scraper construction onto the outcoupling mirror (BB07-E03, Thorlabs). Additionally, apertures are installed before the curved mirrors (not shown in the figure) to avoid back-reflections hitting the mirror mounts. The cell length is roughly adjustable with a moveable adapter for the mirror mount (POLARIS-K50S4/M, Thorlabs) of the second curved mirror. The fine adjustment is done with a translation stage (custom UHV version of 9062-COM-M, Newport) covering 12.7 mm below the first curved mirror. Similarly, the crystal mount is adjustable by the same stage model. Rotary feedthroughs allow stage adjustments in closed cell operation. Cooling of the curved mirrors and the crystal mount is ensured by cooling clamps with copper links. Further, the main

structure can be water-cooled with channels in the bottom. The spot pattern on the curved mirrors can be imaged from the top with silver mirrors and the upside monitoring windows in Figure 3.4 with a camera.
Exiting the MPC is similar: A mirror (Turning mirror 45°, 141501, Layertec) guides the beam through two lenses, (lens 4, LA4874-B $f = 150\,\mathrm{mm}$, Thorlabs) and (lens 5, LA4513-B $f = -75\,\mathrm{mm}$, Thorlabs) for collimation before the post-compression set-up.

As a nonlinear material, we employ YAG elements (undoped YAG111, ⌀25 mm, AR$<$ 0.15% at 1005 nm to 1055 nm, Item M0058641, Altechna) with thicknesses of 5 or 6.6 mm, or combinations thereof. YAG has an optical Kerr coefficient of $n_2 = 6.2 \times 10^{-16}\,\mathrm{cm}^2/\mathrm{W}$, which is more than twice that of fused silica [31]. The critical power of YAG is 1.5 MW [31], which our laser pulse would exceed with an average power starting from 30 W, assuming a pulse duration of 200 fs.

3.3 FROG set-up

A FROG set-up requires the generation of a variably delayed pulse copy. Therefore, I adapted an existing split-and-delay (SAD) line in our experiment, detailed in the next section. Further, I designed and built a compact breadboard containing the FROG components, described thereafter.

3.3.1 Split-and-delay line

Our experiment contains a SAD line based on a Mach-Zehnder interferometer for pump-probe experiments with polarisation shaping [10]. The for interferometric FROG adapted version is shown in Figure 3.6.
The incoming pulse with tunable polarisation enters the box in the upper right corner onto a 50:50 beamsplitter cube (BS011, Thorlabs). The transmitted part passes a waveplate which is used to fine tune its polarisation such that both FROG pulses have the same intensity. Next the transmitted part is variably delayed in a retroreflector consisting of two mirrors (BBSQ1-E03, Thorlabs) on top of a

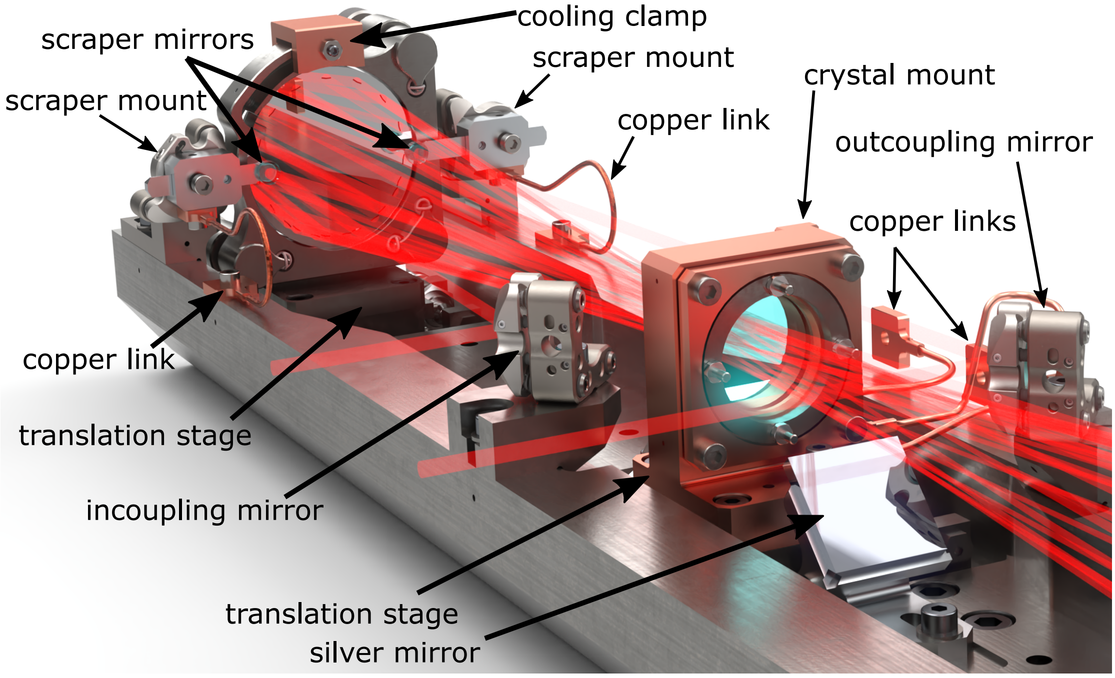

Figure 3.5: Close view of the MPC inside design with exemplary beam path. the incoupling mirror guides the beam (red) onto the small scraper mirror connected with an arm to the scraper mount. Then, the beam propagates back and forth between the curved mirrors and passes through the crystal until it is outcoupled by the second scraper, followed by the outcoupling mirror. The position of curved mirror 1 and the crystal can be fine-tuned with translation stages. The curved mirrors, the scrapers and the crystal mount are cooled by cooling clamps with copper links. The silver mirror is used for imaging the spot pattern on the curved mirror with a camera from above. Adapted from [10].

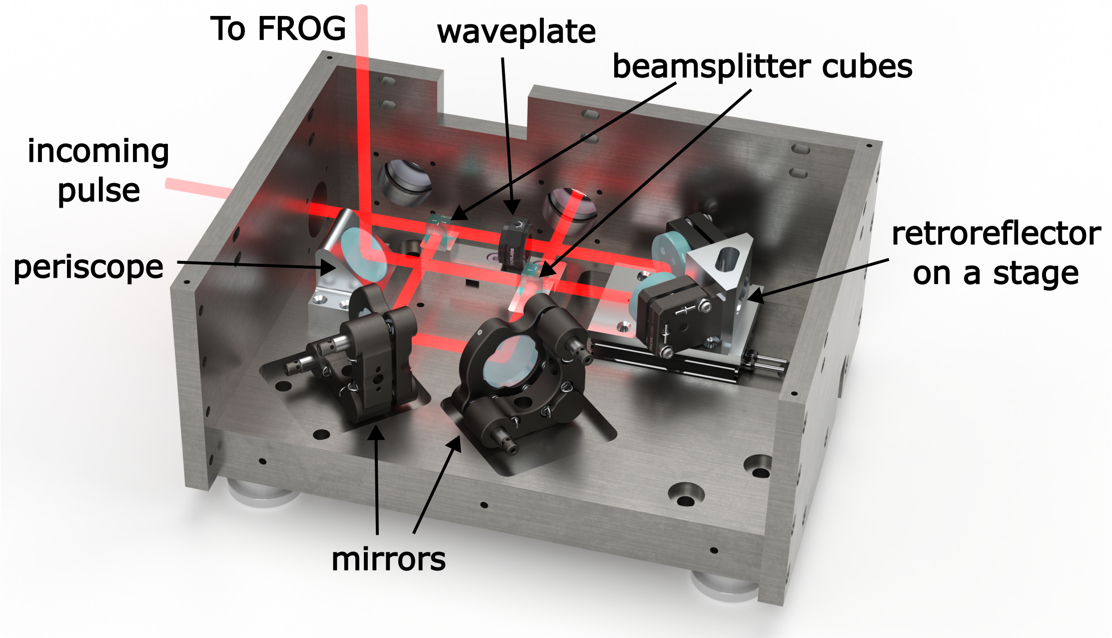

Figure 3.6: Design of the split-and-delay (SAD) line for FROG. The incoming pulses are splitted at a 50:50 beamsplitter cube. The transmitted part passes a waveplate before being variably delayed in a retroreflector on top of a translation stage. The reflected part is guided by two mirrors onto the second beamsplitter cube which mixes both pulse parts again. From the second beamsplitter cube there are two ways to exit the box, upwards onto the FROG breadboard with a periscope or horizontally. Adapted from [10] with the kind help of Yannick Steinhauser.

translation stage (Q-545 Q-Motion® Precision Linear Stage, Physik Instrumente (PI)) with a movement range of 26 mm and step size of 6 nm. The relative time delay τ of a pulse obtained by a stage movement of distance d is $\tau = 2d/c$.
The at the first beam splitter reflected part is guided by two mirrors (Turning mirror 45°, 141501, Layertec) onto the second 50:50 beamsplitter cube (BS011, Thorlabs) which mixes both pulse parts again. From the second beamsplitter cube there are two ways to exit the box, horizontally or upwards onto the FROG breadboard. For the latter, I designed a fixed periscope with a glued-in mirror (Turning mirror 45°, 141501, Layertec) at 45° angle.

3.3.2 FROG breadboard

A breadboard for FROG, to be flexibly attached on top of the SAD line, was designed by me. This setup allows for pulse measurements when needed while conserving space. Figure 3.8 shows the model of the breadboard whose optical set-up is condensed in Figure 3.7. With a home-built periscope, the light pulse $E(t)$ and its time-shifted copy are directed onto the breadboard. The periscope's bottom-part has a broadband dielectric mirror (BB1-E03, Thorlabs) glued in at a 45° angle directing the light upwards. Its top-part can contain one or two separately adjustable mirrors (BBSQ1-E03 in mount KMSS/M, Thorlabs) for interferometric or non-collinear FROG respectively. The **beam height** with respect to the breadboard is **71.7 mm**. To obtain this height the breadboard can be slightly moved in the plane to ensure the upcoming light hits the periscope at the correct beam height. The breadboard position on top of the SAD box can be marked by screwing two metal blocks at the breadboard bottom to the boxes' walls.

The working principle of the FROG breadboard is illustrated in Figure 3.7: First, the light is focused by a lens ($f = 75\,\mathrm{mm}$, LA1608-B, Thorlabs) into a BBO crystal (BBO-652H, EKSMA optics, $\varnothing 12.7\,\mathrm{mm}$) with a thickness of $d = 1\,\mathrm{mm}$. The crystal is mounted in a home-built one-inch mount allowing for a defined rotation in a two-axis crystal mount (POLARIS-K1VS2, Thorlabs). Before the crystal, a polarising beam splitter cube (PBS12-1064-HP, Thorlabs) can be added to filter out the small amount of light whose polarisation changed when passing the beam splitters in the SAD line. This process helps improve the phase-matching of the two pulses. A collimation lens ($f = 75\,\mathrm{mm}$, LA1257A, Thorlabs) guides the light to a dielectric mirror (DMSP1500, Thorlabs). The mirror transmits a 95% of the infrared and reflects the generated SHG onto a fiber coupler (PAF-X-15-A, Thorlabs). A single-mode fiber (custom made SM450 FC/APC to SMA) transmits the green SHG light to a spectrometer. We employ an off-the-shelf spectrometer (Qmini VIS, AFBR-S20M2VI, Broadcom) or a home-built echelle-grating spectrometer [24] which is detailed in the next section.

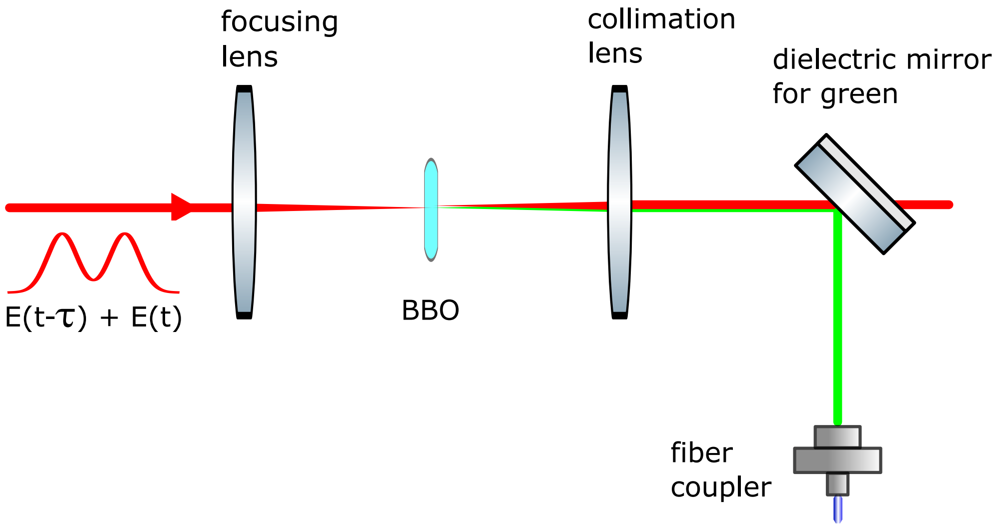

Figure 3.7: Schematic optical set-up of the FROG breadboard. The light pulse $E(t)$ and its by τ time-shifted copy are focused into a BBO crystal for SHG. A collimation lens guides the light to a dielectric mirror which transmits the main part of the infrared and reflects the green second harmonic onto the fiber coupler. Adapted from [24].

3.3.3 Spectrometer

To resolve the second harmonic a home-built Czerny-Turner-Spectrometer is employed. Its description follows [24]. In Figure 3.9, the optical scheme and design of the spectrometer are shown. The second harmonic is incoupled into the aluminium box of the spectrometer with a single-mode fiber (P2-460B-PCSMA-1) with 4.2 μm mode diameter. It hits a prism mirror (MRA20-E02, Thorlabs Inc.), passes a bandpass filter (wavelengths range 485 nm – 565 nm, FGV9, Thorlabs Inc.) and is collimated by a first curved mirror (600 mm radius of curvature, 092-0125R-600, EKSMA Optics). An echelle grating with a line density of 92 mm^{-1} at an angle of incidence of about $\pi/2$ spectrally resolves the colours. A second curved mirror (600 mm radius of curvature, CM750-500-P01, Thorlabs Inc.) collimates the spectrum onto a line camera (pixel size: 14 µm × 56 µm, LC100, Thorlabs Inc.). The line camera is operated by a home-written python library and records a 2048 pixel spectrum.

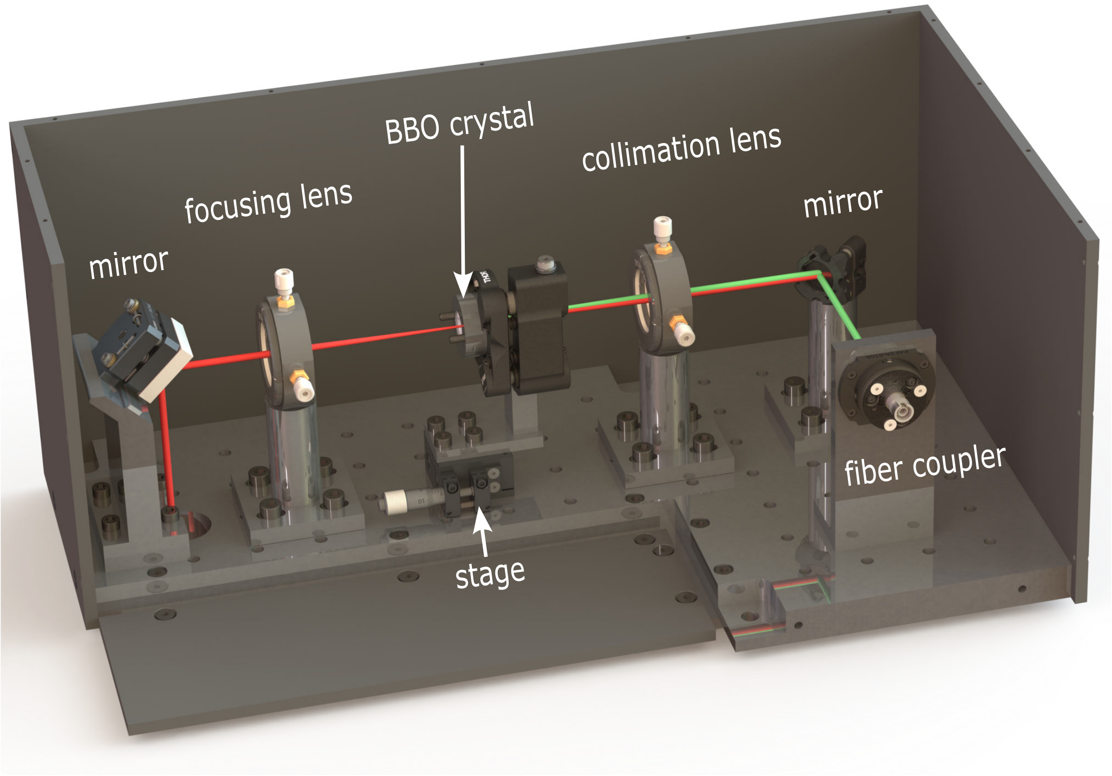

Figure 3.8: Design of the FROG breadboard with beam path for interferometric FROG. The upcoming infra-red laser pulse and its time delayed copy (red, left-side) are reflected horizontally by an adjustable mirror. A focusing lens focuses the pulses onto a BBO crystal in a rotable mount on top of a translation stage. The thereby generated SHG is shown in green. Only the SHG part of the collimated light is reflected on a dichroic mirror, then guided to a fiber coupler.

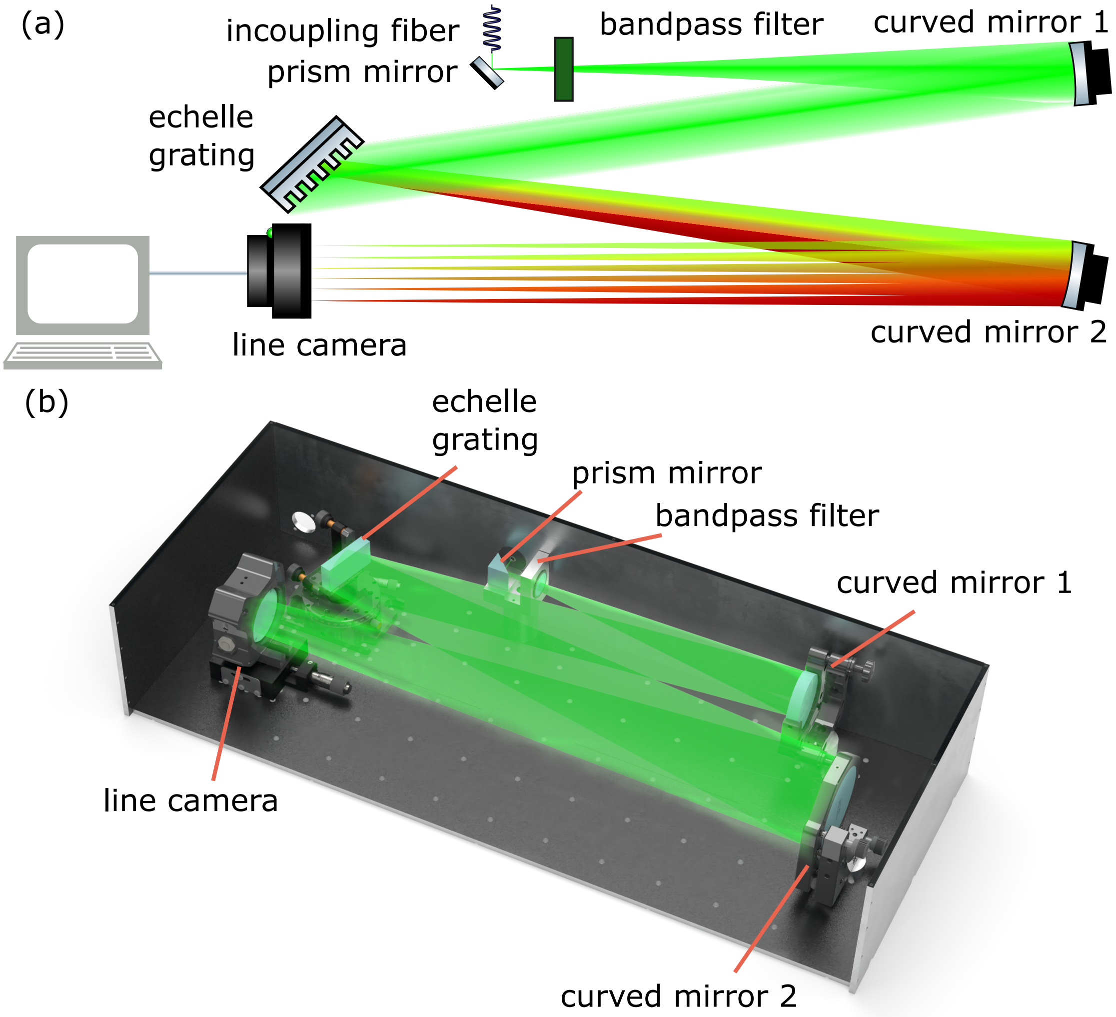

Figure 3.9: Schematic overview a) and design b) of the home-built Czerny-Turner-Spectrometer. The fiber-incoupled light hits a prism mirror, is bandpass filtered and reflected on a first curved mirror towards the echelle grating. Here the spectral components are reflected under a slightly different angle and mapped by a second curved mirror onto a line camera. Adapted from [24].

Calibration

The spectrometer has been calibrated with an Iron-Neon calibration lamp (P826, Photron Pty Ltd.). The recorded spectrum, an average of 10 scans with an integration time of 400 ms, is shown in Figure 3.10. The peaks have been fitted by Gaussian distributions in order to determine the pixel number of the maxima which are indicated by grey lines in the plot. To relate the pixel positions to wavelengths for the second x-axis, a quadratic regression has been done in Figure 3.11. The peak around 1650 pixels has not been taken into account as its shape deviates from a Gaussian and there is no corresponding transition in the FeNe spectrum. The other peaks could be related to the literature values of [43].
A quadratic regression of Figure 3.11 yields the wavelength λ in dependence of the pixel position x

$$\lambda(x) = -1.229 \cdot 10^{-7} \frac{\mathrm{nm}}{px^2} \cdot x^2 + 8.193 \cdot 10^{-3} \frac{\mathrm{nm}}{px} \cdot x + 511.970\,\mathrm{nm} \tag{3.1}$$

with a quadratic mean squared error of 4.2×10^{-2} nm.

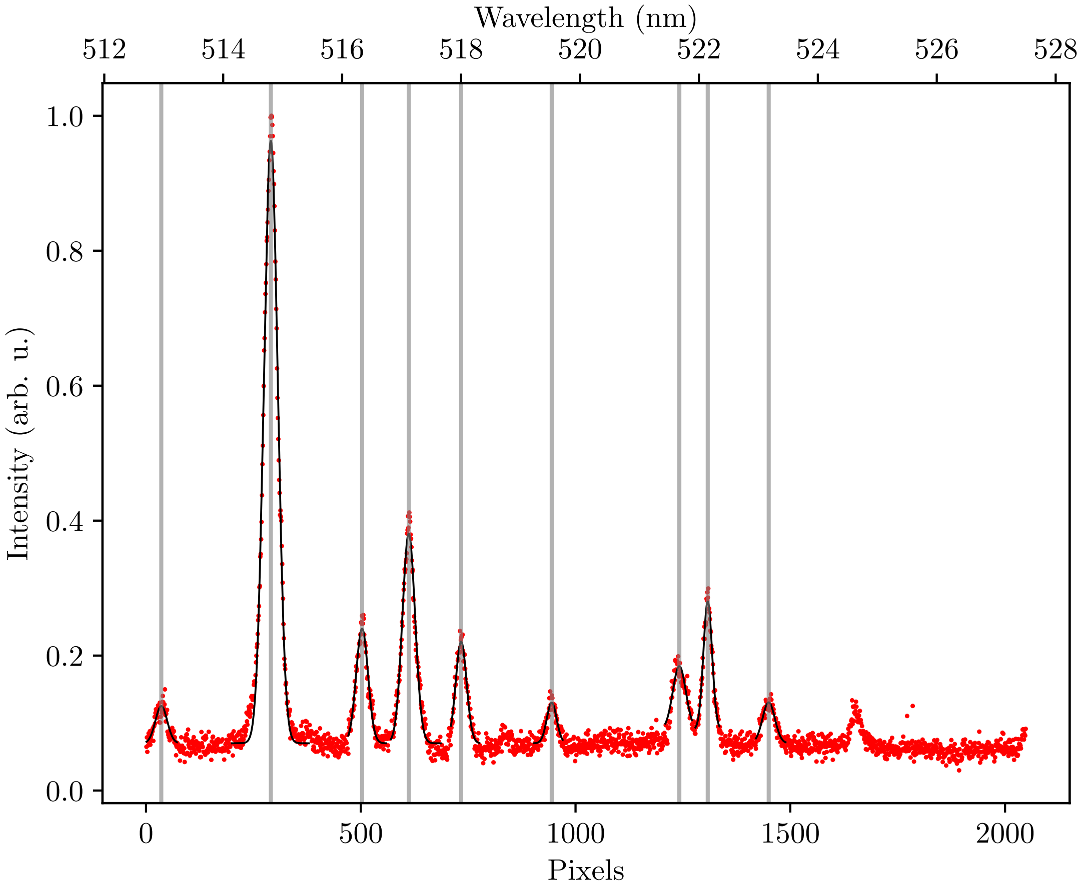

Figure 3.10: Calibration of the Czerny-Turner-Spectrometer with the spectrum of a FeNe-Lamp. Red spectrum recorded with 400 ms integration time of the line camera and averaged over 10 scans. The peaks are fitted with Gaussian functions whose maximum is indicated by the grey vertical lines. (The peak around 1650 pixels was not used as its shape deviates from a Gaussian and there is no corresponding transition in the spectrum of FeNe.) Comparing the spectrum to the theoretical expectation [43] yields the corresponding wavelength axis.

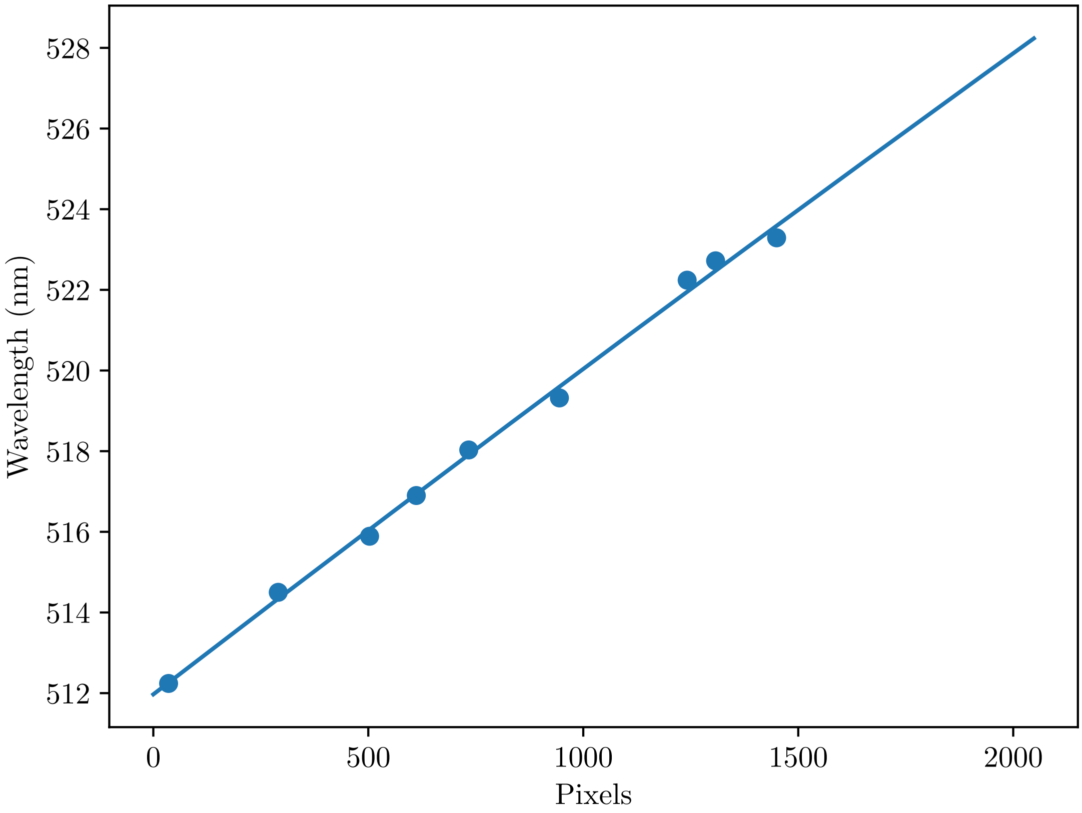

Figure 3.11: Calibration of the Spectrometer with the spectrum of a FeNe-Lamp. The quadratic regression relates the in Figure 3.10 determined pixel values of the peaks to their literature values from [43].

4 Results and Discussion

4.1 Pulse characterisation before the MPC

In this section the laser pulse is characterised after the pulse preparation stage, explicitly after the grating compressor (see Figure 3.1). In the following this measurement position will simply be called "before the MPC". The pulse characterisation is effected firstly with a commercial autocorrelator and secondly with the self-built FROG set-up.

4.1.1 Autocorrelation

Figure 4.1 presents the autocorrelation of a commercial autocorrelator (pulseCheck 15, APE). The commercial autocorrelator uses the same measurement principle as a FROG apparatus: One pulse is variably delayed relative to a second pulse, thereafter, they are overlapped in a nonlinear crystal. The power of their second harmonic is measured over the delay. Unlike FROG, this setup does not resolve the power spectrally, requiring an assumption of the pulse shape to estimate the pulse length. A Gaussian profile was assumed in this analysis, yielding a pulse duration of $\tau = (187 \pm 2)\,\mathrm{fs}$. Nevertheless, the Gaussian fit falls short of accurately modeling the low-power regions, suggesting a more complex pulse shape.

4.1.2 FROG

In the following, the FROG results recorded with the self-designed set-up are presented. Starting from a raw FROG trace, first a noise correction is applied and then the retrieval process optimised.

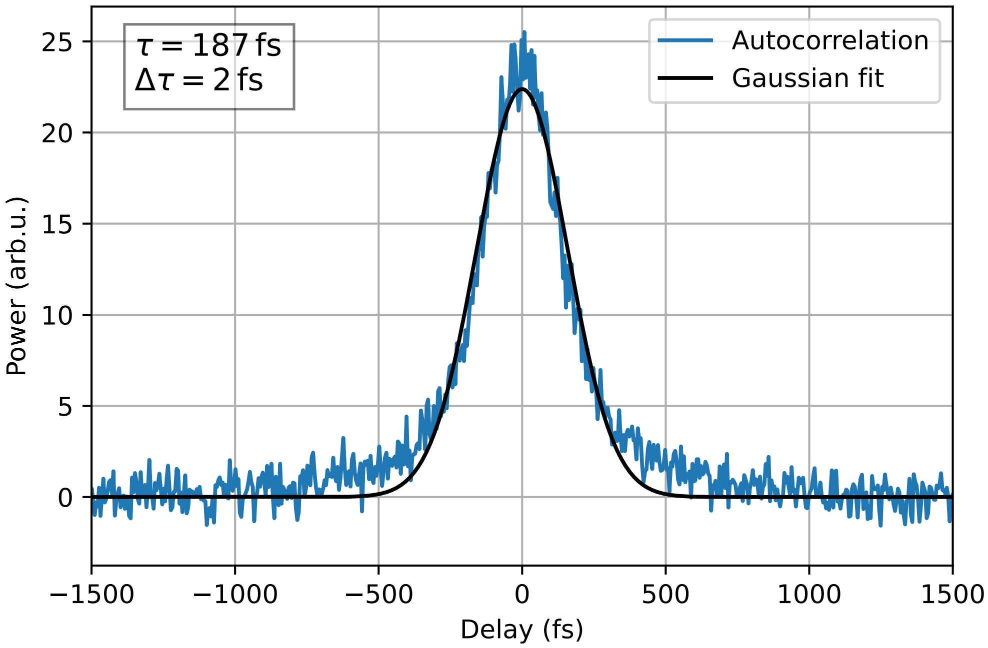

Figure 4.1: Autocorrelation measured before the MPC with a commercial autocorrelator. The SHG power (blue) is depicted over the time delay between the two pulses. Assuming a Gaussian pulse shape (black), the pulse duration is retrieved as $\tau = (187 \pm 2)\,\mathrm{fs}$. Visibly a Gaussian fit does not represent the low power regions properly which indicates a more complex pulse shape. The code for this plot was generated with the assistance of [44].

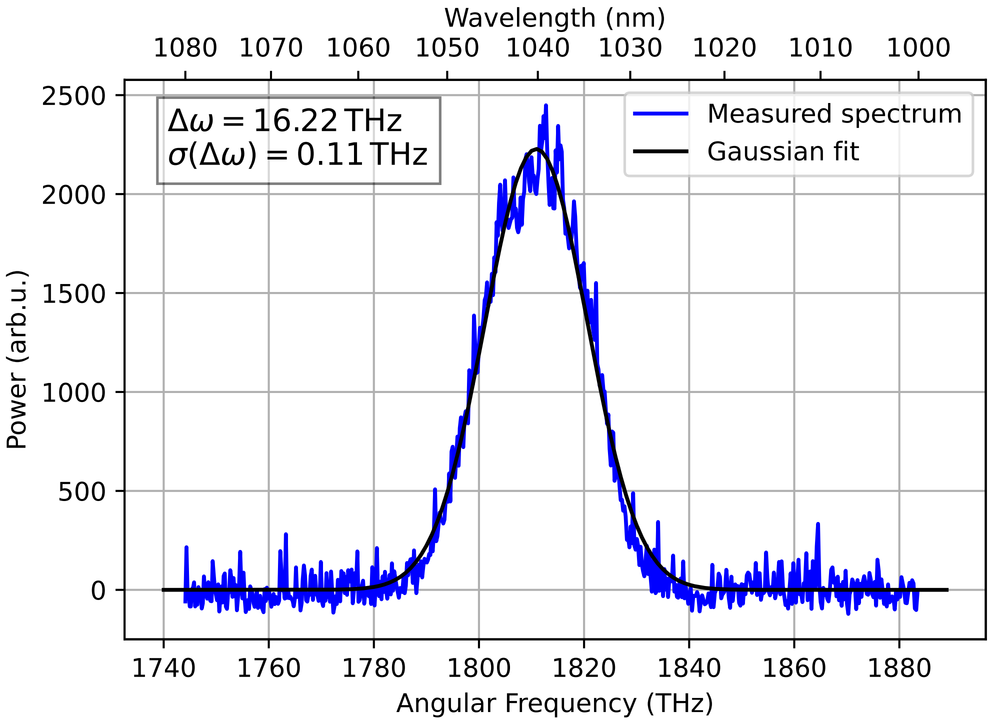

Figure 4.2: Pulse spectrum measured before the MPC. The power (blue) depending on angular frequency ω and corresponding wavelength is fitted by a Gaussian (black) which resulted in a bandwidth of $\Delta\omega = (16.22 \pm 0.11)\,\mathrm{THz}$. This translates to a wavelength bandwidth of $\Delta\lambda = (9.2 \pm 0.2)\,\mathrm{nm}$. The code for this plot was generated with the assistance of [44].

For comparison with the FROG results, a measured pulse spectrum is illustrated in Figure 4.2. The spectrometer (Qmini NIR, AFBR-S20M2NI, Broadcom, spectral resolution 0.8 nm) recorded for each wavelength a corresponding power (blue line). Considering its later detailed use for retrieval optimisation, the spectrum is fitted by a Gaussian (black line) over angular frequency ω. The fit yields a bandwidth of $\Delta\omega = (16.22 \pm 0.11)\,\mathrm{THz}$ which corresponds to a wavelength bandwidth of $\Delta\lambda = (9.2 \pm 0.2)\,\mathrm{nm}$.

The raw FROG trace is shown in the left panel of Figure 4.3. For each delay between the two pulses a spectrum is depicted as a vertical line using a logarithmic colour scale for its intensity values. For the following features, noise corrections have been applied:

Symmetry Symmetry with respect to delay is an inherent feature of an SHG FROG trace. Thus all retrieved traces will be symmetrical, therefore this symmetry is enforced on the measured trace. Firstly, the center of mass of the frequency marginals (Equation 2.46) has been defined as the zero delay symmetry axis. Then, an arithmetic mean of the two values with the same delay distance to this symmetry axis has been employed.

Stray light Since the spectrum around zero delay is broader than in a separate spectral measurement (see Figure 4.2), stray light, especially at high powers, in the spectrometer is the assumed cause. Hence, for each delay column an intensity correction is substracted. This intensity correction is the sum of the 90 least intensities per column which in total contains 4096 intensities. Afterwards, all negative values are set to zero.

Noise The vertical lines and isolated clusters in the raw trace are likely noise or artefacts. However, they could be a part of the trace to some extent since some retrieved traces do contain isolated clusters. Consequently, a balance had to be struck to ensure the elimination of these vertical lines and isolated clusters was sufficiently rigorous, yet not deleting too many trace features. This was done by setting pixels with more than four non-zero neighbors to zero, employed 90 times in a row.

The next step is the pulse retrieval form the noise-corrected trace using the ePIE retrieval algorithm, detailed previously in Figure 2.10. The traces spectrum in Figure 4.3 does not show a Gaussian profile when comparing the estimated integrals over the delay at each wavelength. Hence, the spectrum measured before the MPC from Figure 4.2 is included into the retrieval process with a randomised update strength between 0.05 and 0.08. After 78 iterations the FROG error stabilised at $G = 1.49 \times 10^{-3}$. Figure 4.4 shows a comparison between the thus retrieved trace (b) and the noise-corrected ePIE-input (a). The FROG error alone is not a

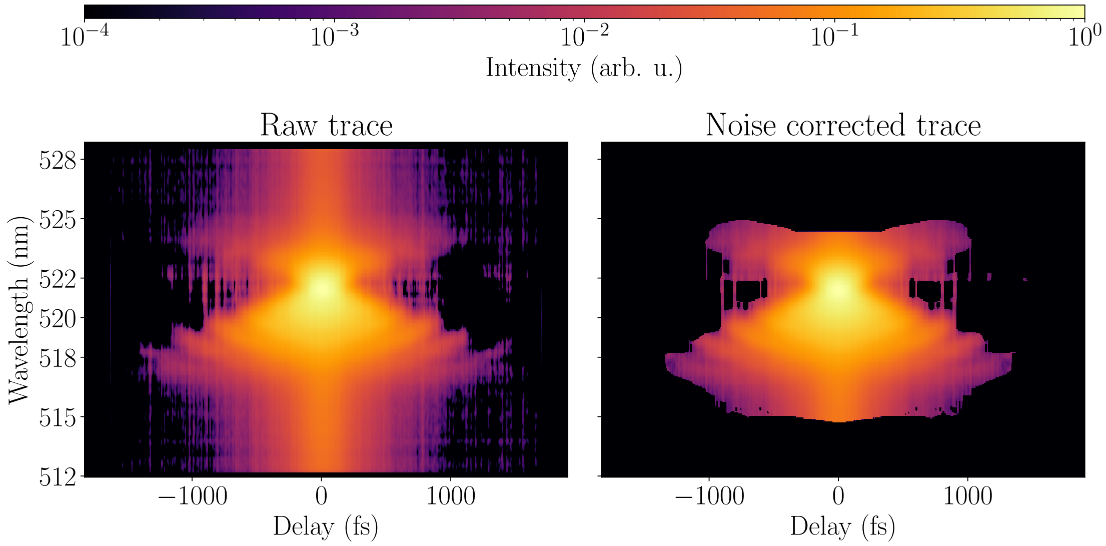

Figure 4.3: Raw trace (left panel) versus noise corrected FROG trace (right panel) measured before the MPC. For each delay between the two pulses a spectrum is depicted as a vertical line using a logarithmic colour scale for its intensity values. The following noise corrections have been applied: To enforce symmetry with respect to zero delay an arithmetic mean is employed. Since the spectrum around zero delay is broader than in a separate spectral measurement (see Figure 4.2), stray light at high powers in the spectrometer is the assumed cause. Therefore, a stray light correction has been applied, which subtracts in each column (containing 4096 values) its 90 least values, then setting negative values to zero. The vertical lines and isolated clusters in the raw trace are likely noise or artefacts, but could to some extent be a part of the trace. Thus, a noise clean-up setting pixels with more than four non-zero neighbors to zero has been employed 90 times in a row. The code for this plot was generated with the assistance of [44].

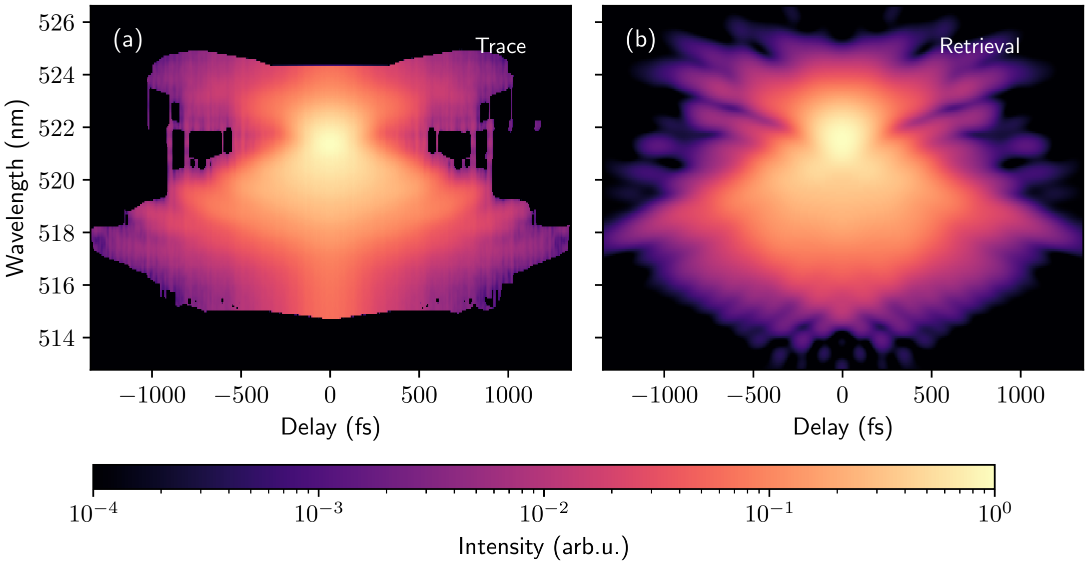

Figure 4.4: Noise corrected FROG trace from 4.3 (a) with its corresponding retrieved trace (b) using the ePIE algorithm with the option of including the spectrum measured before the MPC (see Figure 4.2) into the retrieval process with a random update strength between 0.05 and 0.08. After 78 iterations the FROG error stabilised at $G = 1.49 \times 10^{-3}$. The retrieved trace resembles the original, though there are differences in the fringes. The code for this plot was generated with the assistance of [44].

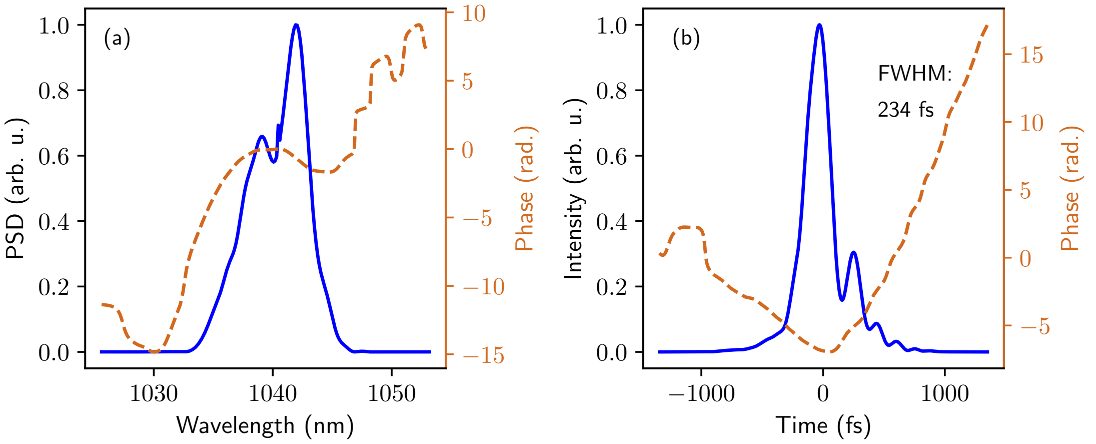

Figure 4.5: The retrieved pulse shape corresponding to the noise-corrected raw trace in Figure 4.3 is depicted in the spectral (a) and temporal domain (b). In (a) the pulse's spectral density (PSD) (blue) shows a dip at around 1040 nm in contrast to the expected Gaussian distribution. Some features vary from retrieval to retrieval: The depth of the dip (by about 100%), the form of the peak at about 1039 nm and the height of the thin peak at about 1041 nm (by about 200%). The latter is the peak of the spectrum measured before the MPC included in the retrieval process. The spectral phase (orange dotted in (a)) and the temporal phase (orange dotted in (b)) most resemble the theoretic case of a cubic spectral face in Figure 2.9. The intensity distribution (blue in (b)) determines a full width at half maximum (FWHM) of 234 fs from the width without employing a fit. For 19 retrievals of this trace, the pulse duration remains in the interval 210 fs to 240 fs. Further a train of post-pulses which is ambiguous to a train of pre-pulses. The code for this plot was generated with the assistance of [44].

sufficient criterion for the retrieval's accuracy. Due to this, the visual agreement between input and retrieved trace needs to be analysed. This analysis is combined with the analysis of the retrieved pulse shape in Figure 4.5. (a) shows the power spectral density (PSD) (blue line) and spectral phase (orange dotted line) over the wavelength. In (b) the corresponding intensity (blue line) and phase (orange dotted line) are depicted in the temporal domain. A full width at half maximum (FWHM) of 234 fs is deduced from the temporal width without employing a fit. It varies from retrieval to retrieval in the range 210 fs to 240 fs.

At delay zero, the maximum intensity of the retrieved trace, with respect to the noise-corrected raw trace, is shifted by approximately 0.3 nm to ~ 521.5 nm. This leads to a maximum PSD at about 1043 nm in Figure 4.5 (a). Whereas, in the spectrum measured before the MPC (see Figure 4.2) the maximum intensity is at 1040.2 nm which is more than 2 nm lower than in the noise-corrected raw trace.

At 1040 nm the PSD in Figure 4.5 (a) inhibits a dip. The depth of this dip varies from retrieval to retrieval. Additionally, the shape of the peak at 1039 nm varies slightly from retrieval to retrieval. Thus the retrieval in the wavelength range of about (520.0 ± 0.5) nm is ambivalent. It could be a sign for less reliable data in that wavelength range, which corresponds to a certain pixel range of the line camera in the home-built echelle spectrometer.
At 1041 nm the PSD in Figure 4.5 (a) shows a thin peak. The height of this peak varies significantly, sometimes tripling, from retrieval to retrieval. This variation results from the inclusion of the spectrum measured before the MPC into the retrieval with a randomised update strength.
At 521.5 nm of the noise-corrected raw trace the delay width is with about 1000 fs about 600 fs more narrow than for adjoining wavelengths. This dip in delay width has only been retrieved partially, and its presence is not influenced by the inclusion of the spectrum measured before the MPC in the retrieval process. The delay width dip has no representation in the retrieved PSD as the latter originates from the integral over the delay not the delay width.
The retrieved trace exhibits more features in the fringes compared to the noise-corrected raw trace, suggesting that the noise correction may have eliminated some

inherent characteristics of the fringes. However, since the fringes are at very low intensities, their impact on the retrieval process is likely minimal.
An additional advantage of a FROG measurement over an autocorrelation is the access to phase information. In Figure 4.5, the spectral phase (orange dotted line in (a)) and the temporal phase (orange dotted line in (b)) closely align with the theoretical scenario of a cubic spectral phase in Figure 2.9. A cubic spectral phase comes with a train of post-pulses. It's important to note that a train of post-pulses is indistinguishable from a train of pre-pulses in an SHG FROG.

Upon reviewing the progress made in this work compared to the starting point illustrated in Figure 1.3, the previously observed wavelength-dependent noise is no longer apparent. However, stray light has increased in intensity. Notably, the symmetry of the raw trace has significantly improved. These improvements stem from a shortened path length between the split-and-delay-line and the FROG set-up, which reduces the impact of tip-and-tilt effects on the delay stage. Additionally, employing 50:50 beam splitters instead of polarising beam splitters in the SAD line helps minimise changes in polarisation effects.

In summary, an autocorrelation initially estimated the pulse duration to be $\tau = (187 \pm 2)\,\mathrm{fs}$, suggesting a pulse shape more complex than Gaussian. Symmetry, stray light, and noise corrections were applied prior to pulse retrieval, affecting some inherent trace information.
The retrieved PSD exhibits a maximum near 1043 nm and a dip around 1040 nm, its shape varying across retrievals. This diverges from an independently measured Gaussian distribution peaking at 1040.2 nm. In the temporal domain, the 210 fs to 240 fs long pulse features a train of post- or pre-pulses. This closely resembles the theoretical scenario of a cubic spectral phase as shown in Figure 2.9.

4.2 Pulse compression in the MPC using YAG

This section details the pulse compression results of the MPC with two 5 mm thick YAG plates at its center. Achieving the optimal beam waist at the focus involves balancing a smaller beam waist, which increases spectral broadening, with a larger beam waist, which facilitates easier outcoupling due to fewer spots. A target beam waist at focus of $w_0 = \mathbf{100\,\mu m}$ was chosen, corresponding to a cell length of 493 mm and 11 spots per circle. In the case of $m = 3$, I managed to fit 14 spots on the first curved mirror, excluding the spots on the in- and outcoupling scraper mirrors, resulting in **30 passes**. In the experiment, the beam exhibited a slight ellipticity ($w_{0,x} = 83\,\mu$m, $w_{0,y} = 103\,\mu$m) and experienced slight changes in collimation with increasing power (an increase of $4\,\mu$m for a power increase from 0.7 W to 6.4 W).

This cell configuration enables an analysis of power transmission, spectral broadening, and the resulting pulse shape, as discussed in the following sections.

4.2.1 Power transmission

Figure 4.6 presents the power transmission of the MPC with 30 passes through two 5 mm thick YAG plates (represented by orange dots) compared to the empty cell (represented by blue dots) as a function of the input power. The impact of the mode-matching telescope (specifically the in- and out-coupling parts) has been accounted for by assuming no significant power-dependent changes from its baseline transmission of 96.9% at laser powers below 500 mW. An error-bar has been representingly obtained at 30 W by taking into account the power changes during a time span of 20 min and reproducibility.

In the empty cell, the transmission remains relatively steady at around 92%, while in the presence of YAG plates, the transmission decreases by 8% as the input power increases from 12 W to 66 W. This reduction in transmission is likely caused by misalignment of the cell due to the nonlinear Kerr effect and thermal expansion.

Comparing these power transmission results with the starting point, specifically the results obtained with two plates of fused silica in [20], reveals some key differences. First, it should be noted that the MPC configuration varied slightly, featuring a beam waist of approximately $95\,\mu$m and 34 passes. Therefore, the power transmission with two fused silica plates $\sim 81\%$ and in an empty cell $\sim 85\%$ as reported in [20] would be around 2% better for only 30 passes. Thus, overall, the transmission of the empty cell appears to have improved by about 5%. Contrary, the transmis-

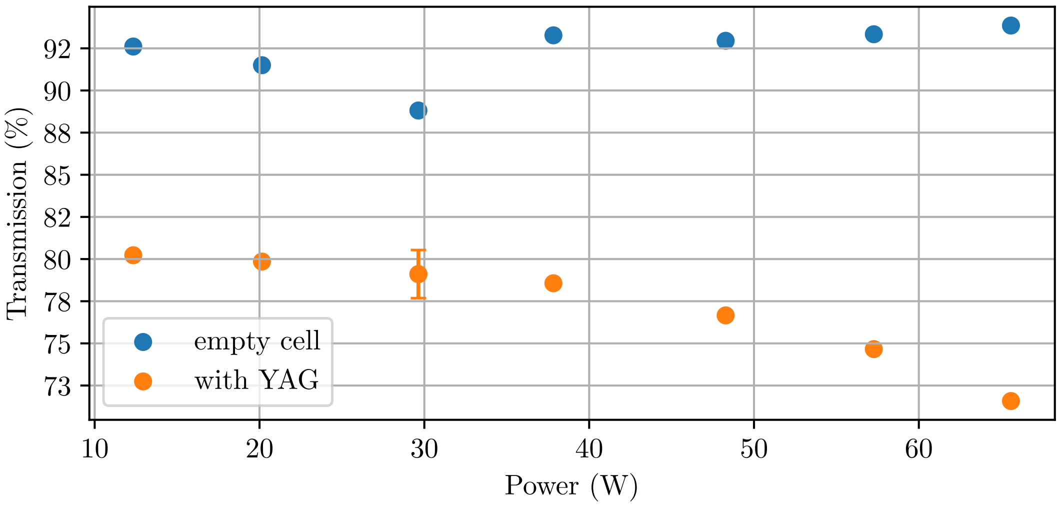

Figure 4.6: Power transmission of the MPC with 30 passes. The transmission of the cell containing two 5 mm thick YAG plates (orange dots) decreases slightly with increasing laser power whereas, the transmission of the empty cell remains approximately constant. The error-bar has been obtained by taking into account the power changes during a time span of 20 min and reproducibility. The impact of the mode-matching telescope (specifically the in- and out-coupling parts) has been accounted for by assuming no significant power-dependent changes from its baseline transmission of 96.9% at laser powers below 500 mW. The code for this plot was generated with the assistance of [44].

sion with substrates is decreased by over 3%. The cause might be different surface properties of the two substrates.

Previously, with fused silica, misalignments occurred at input powers above 55 W, leading to a rapid decrease in output power and making stable operation unattainable [20]. Notably, despite a slight drop in transmission, the cell could still be operated stably up to the maximum possible input power of 66 W. This improvement is probably attributed to the reduction in the number of passes from 34 to 30. As a result, the slight alignment changes due to SPM are less likely to cause clipping at the scrapers.

4.2.2 Spectral broadening

The spectral broadening of the pulse after 30 passes through two 5 mm thick YAG plates is shown in Figure 4.7. The spectra were captured using a spectrometer (Qmini NIR, AFBR-S20M2NI, Broadcom) with a spectral resolution of 0.8 nm, without post-compression. Panel (a) displays the logarithmic PSD for each wavelength, with each colour representing a different incident (or input) power level. The spectra were recorded under various spectrometer settings, so each spectrum has been normalised and scaled according to its respective incident power. Panel (b) presents a logarithmic colour mesh of the PSD for each incident power. This representation highlights the increase in bandwidth as incident power rises. At an incident power of 57.3 W, significant spectral components can be seen across the full 40 nm range. The Gaussian spectral shape evolves into two distinct peaks with side fringes as the incident power increases. The maximum intensity shifts to 1030 nm at 57.3 W.

According to theoretical considerations, what bandwidth gain can we expect?

Given the retrieved pulse duration of 210 nm to 240 nm and an average input power of 58.3 W, the pulse's peak power is calculated as $P_p = (2.50 \pm 0.16)\,\mathrm{MW}$. Using Equation 2.38, the B-integral per pass is $B_{\text{pass}} = 0.190 \pm 0.012\pi$. Applying Equation 2.39 leads to a spectral broadening factor of $b_n = 7.9 \pm 0.6$. Given the bandwidth of the spectrum measured before the MPC as $\Delta\lambda = (9.2 \pm 0.2)\,\mathrm{nm}$, the theoretical expectation for the output bandwidth is $(72.7 \pm 6.5)\,\mathrm{nm}$. However, as shown in Figure 4.8, we are far from this theoretical expectation. The band-

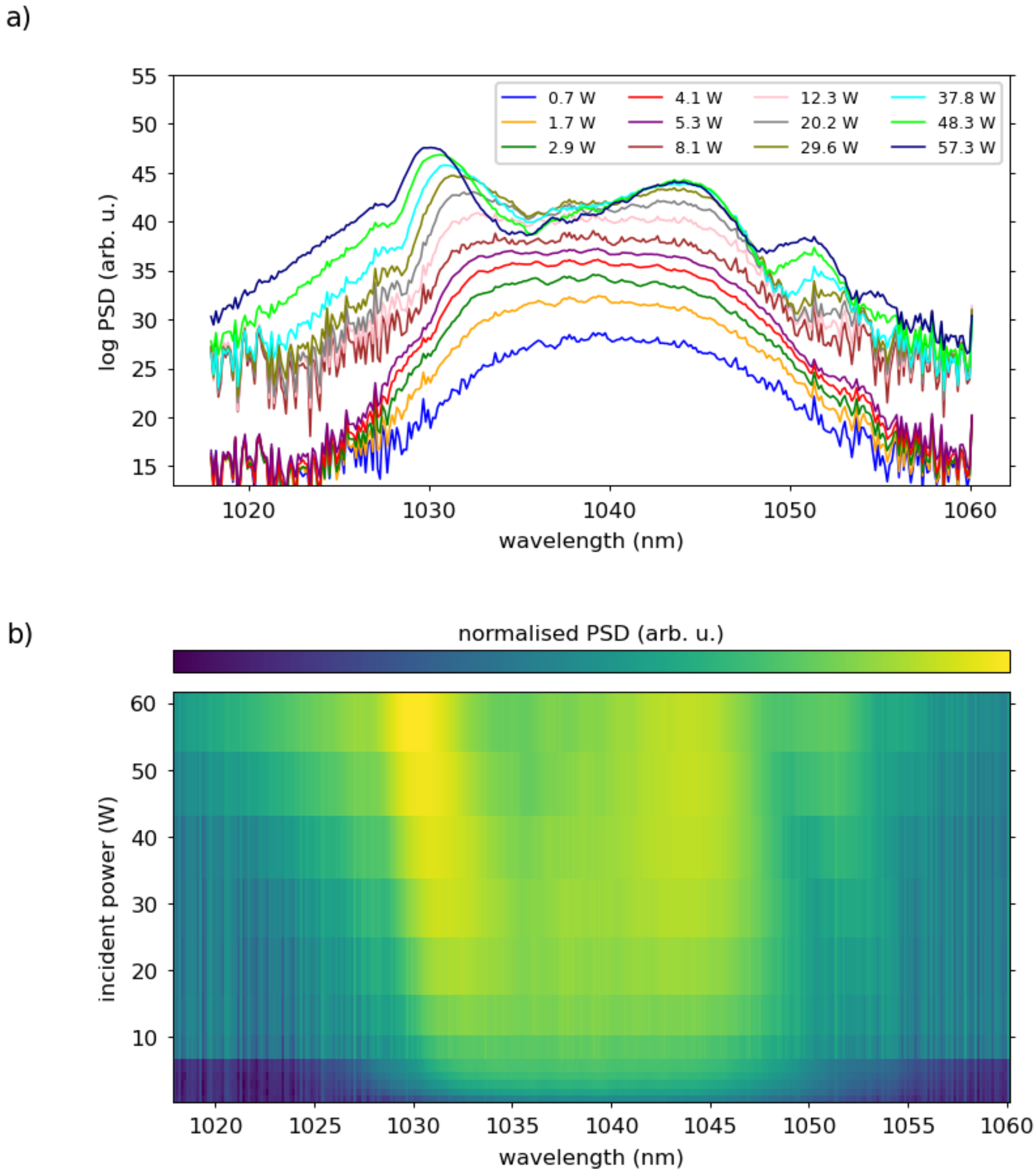

Figure 4.7: Spectral broadening in the MPC using two YAG plates with a combined thickness of 10 mm. In a) the power spectral density (PSD) is shown across the wavelength spectrum, with different colors representing varying incident power levels. As the incident power increases, notable effects are observed: side fringes emerge, the bandwidth expands, and there is a shift in the maximum of the PSD. In b) these features are visualised in a colour mesh. For each combination of wavelength and incident power a logarithmic colour scale denotes the normalised PSD. The code for this plot was generated with the assistance of [44].

width, previously defined as full width at half maximum, is not an appropriate measure for evaluating the spectrally broadened shape. Likely, the chirp per pass has not been adequately compensated, resulting in a reduction of pulse peak power and significantly lowering the spectral broadening effect with each pass. Further, imprecise mode-matching might reduce the obtained spectral broadening. Imprecision in mode-matching can result from the power-dependent Kerr lensing, but also from a power-dependent change of the input beams focus size and position or from the beam's ellipticity.

This paragraph evaluates the obtained spectral broadening in comparison with the initial starting point—the fused silica results from [20]. Figure 4.8 presents a comparison plot of the earlier results with 34 passes through two slightly off-centered 6.35 mm thick fused silica plates at an input power of 54.1 W, compared to my YAG results.

The spectra are normalised to their total power density (area under the PSD curve), with their PSD plotted against wavelength. My main result, involving 30 passes through two 5 mm thick YAG plates at an input power of 57.3 W, is illustrated as the yellow shaded area. As a measure for the spectral broadening the standard deviation σ is employed, which is related to the FWHM of a Gaussian by $\sigma \approx \mathrm{FWHM}/2.355$ [45]. Thus $\sigma = 3.9\,\mathrm{nm}$ for the initial pulse before the MPC of Figure 4.2. In comparison, the main result with $\sigma = 8.3\,\mathrm{nm}$ is more than twice broader.

The input power varies slightly among the different results, making it essential to estimate the input power dependence. Thus, the same configuration with 16% less input power is represented by the sandy brown line, showing slightly reduced PSD in the wings and an increase in maximum wavelength position by approximately 1 nm. This spectrum with $\sigma = 7.7\,\mathrm{nm}$ bears a closer resemblance to the yellow shaded main result than the other spectra, despite the highest input power difference. Hence, slight variations in input power do not significantly affect the main findings of this comparison. Under the same theoretical MPC configuration, but without improvements in mode-matching and prior beam collimation, the use of one 6.6 mm thick YAG plate (chocolate brown line) leads with $\sigma = 6.7\,\mathrm{nm}$ to significantly less broadening.

Additionally, another improvement, the use of chirped curved mirrors in the cell,

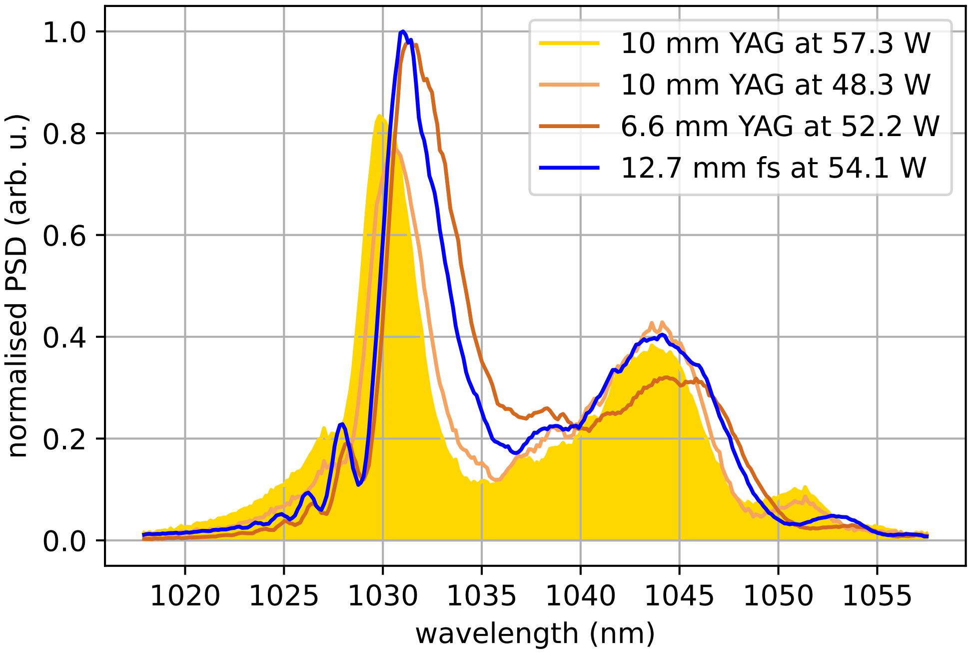

Figure 4.8: Comparison of different spectral broadening results in the MPC. The normalised PSD is plotted against wavelength, with my primary result—30 passes through two 5 mm thick YAG plates at an input power of 57.3 W—illustrated as the yellow shaded area. To assess the dependence on input power, the same configuration with 16% less input power is shown by the sandy brown line, resembling the primary result the most. The use of one 6.6 mm thick YAG plate with 9% less input power (chocolate brown line) reduces a measure for spectral broadening, the standard deviation, from 8.3 nm to 6.7 nm.
34 passes through two slightly off-centered 6.35 mm thick plates of fused silica (blue line) at 6% less input power exhibit slightly more broadening than the single YAG plate, but with $\sigma = 7.2$ nm still 15% less than the primary result with two YAG plates. Fused silica results from [20]. The code for this plot was generated with the assistance of [44].

had not yet been implemented in the following fused silica results from [20]. 34 passes through two slightly off-centered 6.35 mm thick plates of fused silica (blue line) at 6% less input power exhibit with $\sigma = 7.2\,\text{nm}$ slightly more broadening than the single YAG plate, but still 15% less than my primary result with two YAG plates.

Overall, the various improvements and the switch from fused silica to YAG have successfully achieved the goal of increasing spectral broadening; the standard deviation increased by 15%.

4.3 Pulse characterisation after the MPC

In this section, the MPC compressed pulse is characterised using the FROG set-up. As previously described, in the MPC the pulses pass through two YAG plates with a total thickness of 10 mm, 30 times. Subsequently, a wedge (BSF10-B, Thorlabs) reflects 0.6% of the outgoing pulse power into the FROG setup without any prior post-compression. The FROG trace, shown in Figure 4.9, was recorded with an off-the-shelf spectrometer (Qmini VIS, AFBR-S20M2VI, Broadcom) with a spectral resolution of 0.8 nm, at an MPC input power of 57 W. The spectrometer was changed, because the spectrum exceeded the current calibration range, 512 nm to 528 nm, of the home-built echelle spectrometer. This change of spectrometer reduced the number of data points per spectrum from 2048 to 215. The trace's intensity is depicted on a logarithmic scale for each combination of delay and wavelength. Here, the delay axis is not centered at the center of mass of the delay marginal as for all previous cases, but at the previously determined zero delay position. The wavelength range of the trace is broader, approximately 25 nm, compared to the previous range of about 9 nm (see Figure 4.2). The most notable observation is the asymmetry of the trace with respect to zero delay, which is unexpected in an SHG trace.

The only known cause of such asymmetry is spatial chirp, as described by S. Akturk and colleagues [46]. They established that a linear spatial chirp results in a shear of the trace; however, the observed trace in this case appears more complex, suggesting the presence of a nonlinear spatial chirp. The wedge in our set-up after the MPC might introduce a spatial chirp; if this occurs, it is observed only for the broadened spectrum at higher powers. Further investigation is required to understand and eliminate this chirp from the trace to apply the retrieval algorithm. To sum up, the FROG trace is asymmetric only for the compressed pulse at high input powers, associated with a spatial chirp.

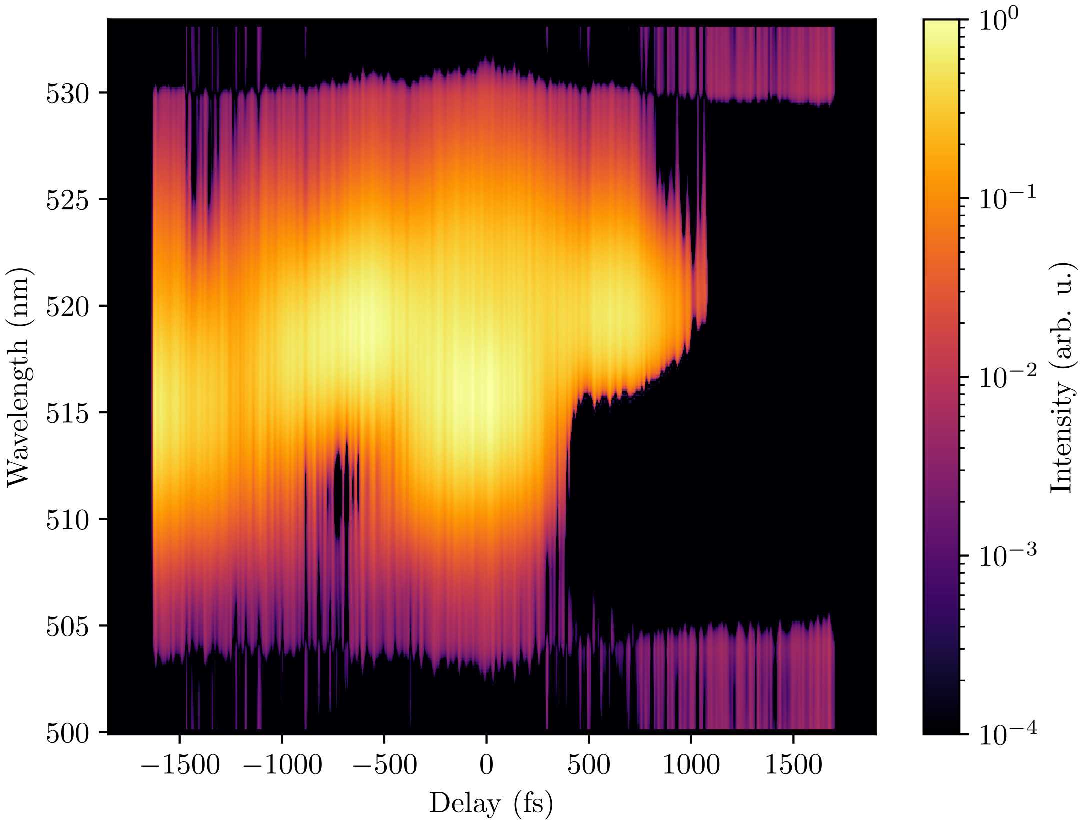

Figure 4.9: FROG trace after the MPC with two YAG plates with a total thickness of 10 mm and an input power of 57 W. For each delay between the pulse copies and each wavelength the corresponding intensity is depicted by a logarithmic colour scale. The wavelength range of the trace is broader, approximately 25 nm, compared to the previous range of about 9 nm (see Figure 4.2). Consequently, this trace was captured using an off-the-shelf spectrometer, offering 215 values per spectrum, rather than the home-built echelle spectrometer.A notable feature of this trace is the asymmetry with respect to zero delay, which is unexpected in an SHG trace. The only known cause of such asymmetry is a spatial chirp, as described in [46]. Further investigation is required to understand and eliminate this chirp from the trace to apply the retrieval algorithm. The code for this plot was generated with the assistance of [44].

5 Conclusion and Outlook

This research aimed to optimise the pulse compression within a MPC through pulse characterisation by FROG. A pulse duration of 210 fs to 240 fs with post-pulses results in an achievable pulse peak power in the MPC of about 2.5 MW, notably lower than the previously estimated 4 MW [10]. Employing YAG instead of fused silica increases nonlinear effects, thus improving spectral broadening.

Comparing the FROG traces for pulse characterisation with the starting point (Figure 1.3), it is evident that their symmetry and noise level have significantly improved. The observed pulse shape can be attributed to the scenario of a cubic spectral phase in Figure 2.9. In future experiments, it might be advantageous to align the FROG in a non-interferometric setup for faster data acquisition.
The temporal pulse compression in our MPC had begun with a minimal pulse duration of $\sim$ 90 fs at 55 W input power [20] aiming for 30 fs. Improvements in mode-matching, alignment and changing to curved mirrors with a higher reflectivity increased the power transmission of the empty cell by $\sim$ 5% to 92%. Transitioning from fused silica to YAG, which boasts a more than twofold higher optical Kerr coefficient [31], increases the necessity for a direct chirp compensation. Hence, the new curved mirrors were designed for this purpose with a GDD of $-200\,\mathrm{fs}^2$ each. Additionally, the cell's output power is now stable up to the maximum input power of 66 W, likely attributed to reducing the number of passes from 34 to 30. The MPC has more than doubled the pulse's spectral width. Compared to the previous results with fused silica, spectral broadening increased by 15%, although it remains notably below theoretical expectations. This discrepancy suggests firstly, that the per-pass chirp compensation provided by the curved mirrors is insufficient for the 10 mm thickness of YAG, resulting in significant reductions in the pulse's peak power and consequently, the Kerr effect. Hence, exploring options such as reducing the thickness of YAG warrants further investigation. Secondly,

inaccuracies in mode-matching affect the spectral broadening. Thus, a future direction of work involves monitoring power-dependent changes in mode-matching by imaging the transmission of the second curved mirror and compensating for them.

A FROG trace of the pulse after the MPC without a post-compression revealed a notable asymmetry with respect to zero delay. This asymmetry is attributed to a spatial chirp, likely of a nonlinear nature. Investigating and understanding this spatial chirp before implementing post-compression techniques is advisable.

Generally, the pulse characterisation has shown that the pulse's peak energy, at 2.5 MW, remains below the critical power of self-focusing for fused silica, 4.3 MW [31]. Implying that conventional waveguides could serve as a viable alternative to our MPC. However, future plans to introduce a new fiber amplifier before pulse compression will surpass the peak powers compressable by waveguides, thus necessitating the continued use and optimisation of the MPC.

Pulse compression in the MPC aims to achieve higher pulse peak powers, thereby increasing the yield of HHG. Through the HHG process, we transition our NIR frequency comb to the XUV region. Thus, a higher HHG yield allows to attain higher harmonic orders. Additionally, the broader spectrum resulting from pulse compression allows us to reach more HCI transitions. The implementation of a FROG set-up paves the way for monitoring the HHG process in real-time with a fast autocorrelation or a FROG trace. Well-characterised carrier light would allow for optimising and error spotting during the HHG process.

These capabilities are a significant advancement in precision spectroscopy on HCI, offering the potential to uncover new insights into the fine-structure constant and atomic clocks. What other fields will benefit from employing high power pulse compression MPCs?

Acronyms

BBO beta barium borate. 8, 19, 51–53

CEO carrier envelope offset. 2

EBIT electron beam ion trap. 5

ePIE extended Ptychographical Iterative Engine. 36, 39, 40, 61, 63, 81

FROG Frequency Resolved Optical Gating. i–iii, 6–8, 33–38, 40, 42, 48–58, 60–63, 66, 73–77, 81, 82

FWHM full width at half maximum. 14, 42, 64, 65, 71

GDD group delay dispersion. 8, 13, 76

GRENOUILLE grating-eliminated no-nonsense observation of ultra-fast laser-light E-fields. 40

GVD group velocity dispersion. 13

HCI highly charged ions. iii, 5, 6, 77

HHG high harmonic generation. iii, 4–6, 43, 44, 77, 81

iFROG interferometric Frequency Resolved Optical Gating. 38

MPC multi-pass cell. i–iii, 6–8, 24, 26–31, 42–49, 58–77, 81, 82

MPIK Max-Planck-Institut für Kernphysik. i, 5

NIR near-infrared. iii, 1, 4, 6, 43, 77

PCGPA Principal Component Generalised Projections Algorithm. 36

PSD power spectral density. 65, 66, 69–72

RANA retrieval amplitude N-grid algorithm. 37

SAD split-and-delay. 48, 50, 51, 66

SHG second harmonic generation. 16–19, 21, 32–38, 40, 42, 51–53, 59, 61, 66, 73, 75, 81

SI spectral interferometry. 40, 41

SPIDER spectral phase interferometry for direct electric-field reconstruction. 40, 41

SPM self-phase modulation. 23, 69

THG third harmonic generation. 40

XUV extreme ultraviolet. i, iii, 4–6, 42–46, 77, 88

YAG yttrium aluminium garnet. ii, iii, 8, 48, 66–73, 75, 76

List of Figures and Tables

Bibliography

[1] W. Demtröder, *Laserspektroskopie.* Springer, 5 ed., 2007.

[2] Y.-M. Yu, B. K. Sahoo, and B.-B. Suo, “Highly charged ion (HCI) clocks: Frontier candidates for testing variation of fine-structure constant,” *Frontiers in Physics*, vol. 11, 2023.

[3] Physikalisch-Technische Bundesanstalt, “Wie genau gehen die Atomuhren der PTB.” `https://www.ptb.de/cms/ptb/fachabteilungen/abt4/fb-44/fragenzurzeit/fragenzurzeit12.html`, accessed January 16, 2024.

[4] S. M. Brewer, J.-S. Chen, A. M. Hankin, E. R. Clements, C. W. Chou, D. J. Wineland, D. B. Hume, and D. R. Leibrandt, “^{27}Al^{+} Quantum-Logic Clock with a Systematic Uncertainty below 10^{-18},” *Phys. Rev. Lett.*, vol. 123, p. 033201, Jul 2019.

[5] T. Bothwell, C. Kennedy, A. Aeppli, D. Kedar, J. Robinson, E. Oelker, A. Staron, and J. Ye, “Resolving the gravitational redshift across a millimetre-scale atomic sample,” *Nature*, no. 602, p. 420–424, 2022.

[6] W. Demtröder, *Electrodynamics and Optics*, vol. 4. Springer, 2019.

[7] J. Basdevant and J. Dalibard, *The Quantum Mechanics Solver.* Springer, 2 ed., 2006.

[8] T. W. Hänsch, “Nobel lecture: Passion for precision,” *Rev. Mod. Phys.*, vol. 78, pp. 1297–1309, Nov 2006.

[9] W. Demtröder, *Atoms, Molecules and Photons.* Springer, 3 ed., 2018.

[10] J.-H. Oelmann, *Highly nonlinear light-matter interaction using cavity-enhanced frequency combs.* PhD thesis, Max-Planck-Institut für Kernphysik, 2023.

[11] J. Nauta, *An extreme-ultraviolet frequency comb enabling frequency metrology with highly charged ions.* PhD thesis, Max-Planck-Institut für Kernphysik, 2020.

[12] P. B. Corkum, "Plasma perspective on strong field multiphoton ionization," *Phys. Rev. Lett.*, vol. 71, pp. 1994–1997, Sep 1993.

[13] P. M. Paul, E. S. Toma, P. Breger, G. Mullot, F. Augé, P. Balcou, H. G. Muller, and P. Agostini, "Observation of a train of attosecond pulses from high harmonic generation," *Science*, vol. 292, no. 5522, pp. 1689–1692, 2001.

[14] Y.-M. Yu, B. K. Sahoo, and B.-B. Suo, "Highly charged ion (hci) clocks: Frontier candidates for testing variation of fine-structure constant," 2023.

[15] P. Micke, S. Kühn, L. Buchauer, J. R. Harries, T. M. Bücking, K. Blaum, A. Cieluch, A. Egl, D. Hollain, S. Kraemer, T. Pfeifer, P. O. Schmidt, R. X. Schüssler, C. Schweiger, T. Stöhlker, S. Sturm, R. N. Wolf, S. Bernitt, and J. R. Crespo López-Urrutia, "The Heidelberg compact electron beam ion traps," *Review of Scientific Instruments*, vol. 89, p. 063109, 06 2018.

[16] J. Stark, C. Warnecke, S. Bogen, S. Chen, E. A. Dijck, S. Kühn, M. K. Rosner, A. Graf, J. Nauta, J.-H. Oelmann, L. Schmöger, M. Schwarz, D. Liebert, L. J. Spieß, S. A. King, T. Leopold, P. Micke, P. O. Schmidt, T. Pfeifer, and J. R. Crespo López-Urrutia, "An ultralow-noise superconducting radio-frequency ion trap for frequency metrology with highly charged ions," *Review of Scientific Instruments*, vol. 92, p. 083203, 08 2021.

[17] E. A. Dijck, C. Warnecke, M. Wehrheim, R. B. Henninger, J. Eff, K. Georgiou, A. Graf, S. Kokh, L. P. K. Sajith, C. Mayo, V. M. Schäfer, C. Volk, P. O. Schmidt, T. Pfeifer, and J. R. C. López-Urrutia, "Cold highly charged ions in a radio-frequency trap with superconducting magnetic shielding," 2023.

[18] A. Rundquist, C. G. Durfee, Z. Chang, C. Herne, S. Backus, M. M. Murnane, and H. C. Kapteyn, "Phase-matched generation of coherent soft x-rays," *Science*, vol. 280, no. 5368, pp. 1412–1415, 1998.

[19] A.-L. Viotti, M. Seidel, E. Escoto, S. Rajhans, W. P. Leemans, I. Hartl, and C. M. Heyl, “Multi-pass cells for post-compression of ultrashort laser pulses,” *Optica*, vol. 9, pp. 197–216, Feb 2022.

[20] P. Nagpal, “Nonlinear pulse compression in a dispersion tunable multi-pass cell,” Master’s thesis, Max-Planck-Institut für Kernphysik, 2023.

[21] S. Kokh, “Pulse characterisation by frequency-resolved optical gating for velocity map imaging of xenon,” 2022. Bachelor’s thesis.

[22] B. E. A. Saleh and M. C. Teich, *Fundamentals of Photonics.* John Wiley & Sons, 2013.

[23] J.-C. Diels and W. Rudolph, *Ultrashort Laser Pulse Phenomena.* Academic Press, 2 ed., 2006.

[24] S. Angstenberger, “Design of a setup for flexible, dispersion-compensated nonlinear femtosecond laser pulse compression adapted to an extreme ultraviolet frequency comb,” Master’s thesis, Max-Planck-Institut für Kernphysik, 2021.

[25] R. Photonics, “Group delay dispersion.” `https://www.rp-photonics.com/group_delay_dispersion.html`, accessed May 13, 2024.

[26] R. W. Boyd, *Nonlinear Optics.* Academic Press, 3 ed., 2008.

[27] G. Tamošauskas, G. Beresnevičius, D. Gadonas, and A. Dubietis, “Transmittance and phase matching of BBO crystal in the 3–5 μm range and its application for the characterization of mid-infrared laser pulses,” *Opt. Mater. Express*, vol. 8, pp. 1410–1418, Jun 2018.

[28] G. P. Agrawal, *Nonlinear Fiber Optics.* Academic Press, 5 ed., 2013.

[29] D. Herriott, H. Kogelnik, and R. Kompfner, “Off-axis paths in spherical mirror interferometers,” *Appl. Opt.*, vol. 3, pp. 523–526, Apr 1964.

[30] J. Schulte, T. Sartorius, J. Weitenberg, A. Vernaleken, and P. Russbueldt, “Nonlinear pulse compression in a multi-pass cell,” *Opt. Lett.*, vol. 41, pp. 4511–4514, Oct 2016.

[31] J. Weitenberg, *Transversale Moden in optischen Resonatoren für Anwendungen hoher Laserintensität.* PhD thesis, Rheinisch-Westfälische Technische Hochschule Aachen, 2017.

[32] R. Photonics, "Fourier transform spectroscopy." `https://www.rp-photonics.com/fourier_transform_spectroscopy.html`, accessed May 12, 2024.

[33] Y.-M. Yu, B. K. Sahoo, and B.-B. Suo, "Highly charged ion (HCI) clocks: Frontier candidates for testing variation of fine-structure constant," *Frontiers in Physics*, vol. 11, 2023.

[34] R. Trebino, K. W. DeLong, D. N. Fittinghoff, J. N. Sweetser, M. A. Krumbügel, B. A. Richman, and D. J. Kane, "Measuring ultrashort laser pulses in the time-frequency domain using frequency-resolved optical gating," *Review of Scientific Instruments*, vol. 68, no. 9, pp. 3277–3295, 1997.

[35] K. DeLong, D. Fittinghoff, and R. Trebino, "Practical issues in ultrashort-laser-pulse measurement using frequency-resolved optical gating," *IEEE Journal of Quantum Electronics*, vol. 32, no. 7, pp. 1253–1264, 1996.

[36] P. Sidorenko, O. Lahav, Z. Avnat, and O. Cohen, "Ptychographic reconstruction algorithm for frequency-resolved optical gating: super-resolution and supreme robustness," *Optica*, vol. 3, pp. 1320–1330, Dec 2016.

[37] D. Kane, "Real-time measurement of ultrashort laser pulses using principal component generalized projections," *IEEE Journal of Selected Topics in Quantum Electronics*, vol. 4, no. 2, pp. 278–284, 1998.

[38] G. Stibenz and G. Steinmeyer, "Interferometric frequency-resolved optical gating," *Opt. Express*, vol. 13, pp. 2617–2626, Apr 2005.

[39] P. O'Shea, S. Akturk, M. Kimmel, and R. Trebino, "Practical issues in ultra-short-pulse measurements with GRENOUILLE," *Applied Physics B*, no. 79, pp. 683–691, 2004.

[40] S. Palaniyappan, R. C. Shah, R. Johnson, T. Shimada, D. C. Gautier, S. Letzring, D. Jung, R. Hörlein, D. T. Offermann, J. C. Fernández, and B. M. Hegelich, "Pulse shape measurements using single shot-frequency resolved optical gating for high energy (80 J) short pulse (600 fs) laser," *Rev Sci Instrum*, vol. 81, no. 10E103, 2010.

[41] R. Aboushelbaya, A. F. Savin, L. Ceurvorst, J. Sadler, P. A. Norreys, A. S. Davies, D. H. Froula, A. Boyle, M. Galimberti, P. Oliveira, B. Parry, Y. Katzir, and K. Glize, "Single-shot frequency-resolved optical gating for retrieving the pulse shape of high energy picosecond pulses," *Rev Sci Instrum*, vol. 89, no. 103509, 2018.

[42] R. Trebino, R. Jafari, S. A. Akturk, P. Bowlan, Z. Guang, P. Zhu, E. Escoto, and G. Steinmeyer, "Highly reliable measurement of ultrashort laser pulses," *Journal of Applied Physics*, vol. 128, no. 171103, 2020.

[43] National Institut of Standards and Technology, "Atomic spectra database lines data." `https://physics.nist.gov/cgi-bin/ASD/lines1.pl?spectra=Fe+1%3B+Ne&output_type=0&low_w=512&upp_w=527.5&unit=1&submit=Retrieve+Data&de=0&plot_out=0&I_scale_type=1&format=0&line_out=0&en_unit=0&output=0&bibrefs=1&page_size=15&show_obs_wl=1&show_calc_wl=1&unc_out=1&order_out=0&max_low_enrg=&show_av=2&max_upp_enrg=&tsb_value=0&min_str=&A_out=0&intens_out=on&max_str=&allowed_out=1&forbid_out=1&min_accur=&min_intens=&conf_out=on&term_out=on&enrg_out=on&J_out=on`, accessed January 26, 2024.

[44] "Chatgpt." `https://www.openai.com/chatgpt`, 2024. Accessed: January 20, 2024, version 3.5.

[45] W. M. World, "Full width at half maximum." `https://mathworld.wolfram.com/FullWidthatHalfMaximum.html`, accessed May 18, 2024.

[46] S. Akturk, M. Kimmel, P. O'Shea, and R. Trebino, "Measuring spatial chirp in ultrashort pulses using single-shot frequency-resolved optical gating," *Opt. Express*, vol. 11, pp. 68–78, Jan 2003.

Acknowledgements

I extend my sincere thanks to José for welcoming me to this fascinating project and for accommodating my pursuit of chess alongside it.

I am grateful to Thomas for serving as the second examiner.

Many thanks to Lennart, Jan-Hendrik, Tobias and Prachi for their invaluable guidance and assistance throughout this journey. Being part of the XUV-comb group was a wonderful experience. Thank you to everyone for making it memorable. Special appreciation goes to Lennart and Jan-Hendrik for their meticulous proofreading.

I am indebted to the workshop and construction teams, especially Peter Gahn and Yannick Steinhauser, for their help.

I would also like to acknowledge the assistance provided by ChatGPT for formulations and coding during the preparation of this thesis.

Lastly, heartfelt thanks to my family and friends for their moral support.